Thibault Vervenne[1]
Department of Mechanical Engineering,
KU Leuven,
Leuven 3001, Belgium
e-mail: thibault.vervenne@kuleuven.be

Nic Vermeeren
FIBEr - KU Leuven Core Facility for Biomechanical
Experimentation,
KU Leuven,
Leuven 3001, Belgium

Nele Demeersseman
Department of Mechanical Engineering,
KU Leuven,
Leuven 3001, Belgium

Heleen Fehervary
FIBEr - KU Leuven Core Facility for Biomechanical
Experimentation,
KU Leuven,
Leuven 3001, Belgium

Mathias Peirlinck
Department of BioMechanical Engineering,
TU Delft,
Delft 2600, The Netherlands

Ellen Kuhl
Department of Mechanical Engineering,
Stanford University,
Stanford, CA 94305

Nele Famaey[1]
Department of Mechanical Engineering,
KU Leuven,
Leuven 3001, Belgium
e-mail: nele.famaey@kuleuven.be

Stretching the Limits: From Planar-Biaxial Stress–Stretch to Arterial Pressure–Diameter

Understanding the physiological condition of the vascular system is critical to explain, treat, and manage vascular disease. Numerous experimental and computational studies characterize the mechanical behavior of arterial tissue under controlled laboratory conditions. However, translating this knowledge into physiologically realistic conditions remains challenging. Key difficulties include selecting suitable and relevant test methods, minimizing uncertainty, and ensuring robust model validation. Here, we present a novel integrative approach to translate laboratory experiments on arterial samples into clinically relevant pressure–diameter behavior. We perform controlled planar-biaxial tests on carotid arteries under three stretch ratios and generate axial and circumferential stress–stretch data to calibrate a fiber-reinforced soft tissue model. Using an analytical thick-walled cylindrical model, we predict subject-specific pressure–diameter behavior, informed by arterial prestretches from ring opening experiments. We systematically compare predictions against extension-inflation experiments on tubes from the same artery by applying controlled pairs of axial stretch and inner pressure, while recording outer diameter. We quantify prediction error in absolute and relative stretch regimes and evaluate the importance of the load-free reference dimensions. Results show how planar-biaxial tests probe different stretch regimes compared to extension-inflation deformations, leading to extrapolation of model predictions. We demonstrate how the constitutive material parameters can be fitted to different biomechanical loading conditions, and we assess the sensitivity of the simulations to axial stretch and circumferential prestretch. Only when those key model parameters are accurately captured and their uncertainty propagated, planar-biaxial stress–stretch data can reliably predict arterial pressure–diameter behavior.
[DOI: 10.1115/1.4070124]

Keywords: carotid arteries, planar-biaxial, stress–stretch, constitutive modeling, extension-inflation, pressure–diameter

1 Introduction

Biological tissues exhibit complex structural, compositional, and mechanical behavior, making it challenging to accurately quantify their biomechanical properties. Inverse modeling informed by experimental data offers a valuable approach for estimating these properties, but its reliability depends on careful selection of the appropriate test method, design of a physiologically relevant test protocol, making appropriate model assumptions, and performing robust validation. Factors such as biological variability, nonlinearity, and anisotropy further challenge reliable evaluation. This work focuses on key challenges in mechanical testing and subsequent parameter estimation for the biomechanics of arteries, aiming to contribute to more robust and interpretable material descriptions.

Planar-biaxial testing provides a unique and physiologically relevant method for characterizing the mechanical response of arterial tissue, under controlled multi-axial loading [1]. Unlike uniaxial tests, biaxial loading replicates the simultaneous circumferential and axial stresses experienced by arteries in vivo, offering a more complete picture of wall mechanics. A key advantage of this approach is also its tissue-sparing nature, with only small, flat specimens required.

While planar-biaxial testing provides detailed insight into the material behavior, it does not directly result in a pressure–diameter (P–d) relationship, which remains the clinically most relevant descriptor of arterial compliance and function. Pressure–diameter is especially important for cardiovascular tissue under dynamic
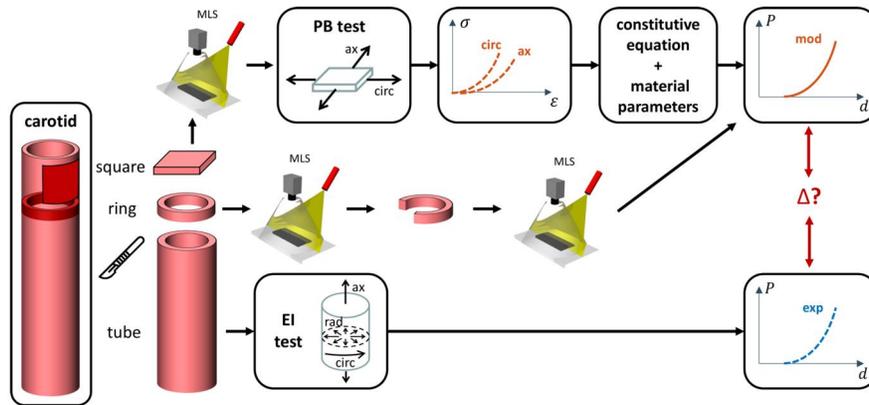
Fig. 1 Experimental and modeled biomechanical characterization workflow. Ovine carotid arteries were prepared for planar-biaxial (PB) loading, ring-opening analysis, and extension-inflation (EI) testing. The axial and circumferential stress–stretch (σ–λ) data from PB testing are used to fit material parameters of a chosen constitutive description. These parameters, combined with wall prestretches derived from the ring-opening analysis, enable the modeling (mod) of pressure–diameter (P–d) behavior. The modeled biomechanical response is then compared to the experimental (exp) P–d curve obtained from EI testing on the same artery. All geometrical measurements were acquired using microlaser scanning.

loading conditions, such as those observed between systolic and diastolic blood pressures. *In vivo*, this pulsatility can be observed through ultrasound, MRI, or 4D-CT imaging [2,3]. Ex vivo pressure–diameter can be captured through extension-inflation testing. Especially for small vessels, planar-biaxial tests are more challenging, and pressure–diameter tests are more intuitive from a mechanoclinical point of view [4]. Nevertheless, extension-inflations suffer from the need for larger tissue sample dimensions and specific testing device requirements.

Stress–stretch data in the axial and circumferential direction is often used to identify suitable constitutive models describing the mechanical behavior of the relevant cardiovascular tissue. Depending on the symmetry and directional dependence observed in the material response, these models may assume isotropic or anisotropic characteristics. From the experimental stress–stretch data, specific material parameters can be estimated through model fitting, allowing the strain energy function to capture the nonlinear mechanical behavior of the tissue. Once calibrated, this constitutive model can be implemented in numerical simulations to predict tissue deformation under physiological conditions. In particular, it enables the computation of pressure–diameter (P–d) responses under simulated extension-inflation scenarios, effectively linking experimental mechanics with computer models [5,6].

Despite the potential to derive clinically relevant insights from mechanical testing and computational modeling, researchers currently face several important challenges throughout this process. First, selecting the most appropriate mechanical testing method, whether planar-biaxial or extension-inflation, is not straightforward. The choice of the experiment depends on the specific output goals, tissue sample, and infrastructure availability. Second, designing a relevant experimental protocol is critical: planar-biaxial testing requires careful control of the axial and circumferential loading paths, while extension-inflation testing invokes simultaneous axial loading and pressurization, a closer approximation of in vivo conditions. Third, minimizing measurement uncertainty is essential, as errors in estimating stress (often due to geometric approximations such as wall thickness and cross-sectional area) and stretch (typically captured via digital image correlation or marker tracking) can significantly affect model calibration. Fourth, selecting appropriate modeling assumptions, including the choice of constitutive model and the boundary conditions applied in simulations, requires a balance between physiological realism and computational tractability. Specifically, axial and circumferential

prestretch can be highly sensitive to modeled pressure–diameter outputs. Finally, robust model validation against independent experimental data is necessary to ensure predictive reliability, while remaining a nontrivial step due to variability in biological samples and limited available data. Each of these aspects demands careful consideration to ensure that experimental and computational findings meaningfully reflect true in vivo tissue behavior.

In this study, we critically evaluate the results of planar-biaxial tensile testing and compare them against the results of extension-inflation tests, aiming to quantify the effects of measurement uncertainty and experimental and modeling design choices.

2 Materials and Methods

Figure 1 schematically illustrates the integrated experimental and computational framework. All mechanical tests and measurements were carried out at FIBEr[2], the KU Leuven Core Facility for Biomechanical Experimentation. The resulting datasets span multiple mechanical tests, processing workflows, and modeling approaches. To promote transparency, reproducibility, and further research, all protocols, raw data, and postprocessing code have been made publicly available.

2.1 Experimental Workflow. Three complementary types of mechanical tests were performed in this study. Planar-biaxial tests were conducted to yield experimental stress–stretch curves, characterizing tissue behavior under controlled axial and circumferential loading conditions. Ring-opening tests were conducted to assess the opening angle, providing insights into the residual stress state and enabling estimation of in vivo arterial prestretches [7]. Extension-inflation tests were performed to generate experimental pressure–diameter data, reflecting the physiological response of the vessels under axial loading and internal pressurization.

2.1.1 Tissue Collection. An overview of the tissue preparation and mounting process is shown in Fig. 2 [8]. Five full-length and fresh ovine carotid arteries, labeled A through E, were collected from one-year-old female Swifter sheep weighing between 50 and 70 kg. The study was approved by the UZ Leuven ethical committee for animal experimentation under protocol number 189/2021. The tissues were harvested and immediately preserved in phosphate-
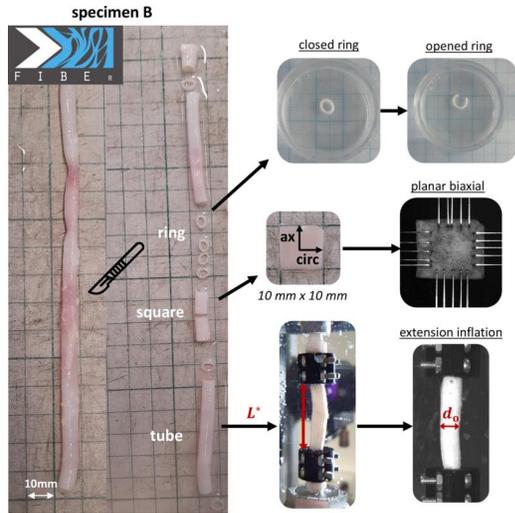
Fig. 2 Schematic overview of tissue harvesting and experimental mounting. Three test samples were prepared from representative specimen B: a square section for planar-biaxial testing, a ring segment for ring-opening analysis, and a tubular segment for extension-inflation testing. The planar-biaxial configuration includes both unmounted and mounted states, with rakes applied in the axial and circumferential directions to impose controlled deformations. The extension-inflation setup illustrates the mounted length L^* and the resulting pressurized outer diameter d_o during testing.

buffered saline at $-80\,°C$ until further use [9]. Prior to testing, samples were thawed gradually in the fridge at $4\,°C$. The whole workflow and results are shown for specimen B as representative example case.

2.1.2 Planar-Biaxial Testing: Experimental Stress– Stretch. We performed planar-biaxial tensile tests using a ZwickRoell (Ulm, Germany) biaxial testing machine for biomaterials on square samples. Five rakes were mounted on each side of the sample, equally spaced, resulting in an initial distance of 7 mm between opposite rake sets in both the axial and circumferential directions. The samples were submerged and tested in a 0.9% saline solution, heated to $37\,°C$. During tensile loading, 30% and 50% stretch levels were applied to the rake holders, calculated relative to their initial positions. Stretches were increased stepwise at a rate of 5%/s until single-rake failure occurred. The planar biaxial setup is equipped with four load cells, each with a capacity of 200 N. The load cells have a resolution of 0.0001 N, and a class 1 accuracy is ensured by the calibration certificate until 0.2% of the capacity of the load cells (0.4 N). This means that the lowest readouts of the load cells have a relative deviation and repeatability precision of 0.004 N (1%), a relative resolution of 0.002 N (0.5%), and a relative zero deviation of 0.0004 N (0.1%). Classification 1 remains valid for loads above the accuracy threshold.

For each loading level, we applied three axial-to-circumferential stretch ratios $\{1:1, 2:1, 1:2\}$ using displacement-driven actuators [10]. A 1:2 ratio indicates that half of the 30% or 50% stretch was applied in the axial direction, while the full stretch level was applied in the circumferential direction. Four preconditioning cycles were performed for each loading step and stretch ratio, and the fifth cycle was used for postprocessing [11], with a machine sampling rate of 20 Hz.

Experimentally measured forces were converted to engineering stresses using the initial load-free thickness and areal sample measurements, obtained before testing via microlaser scanning (Acacia Technology and Gocator Emulator, LMI Technologies, Vancouver, Canada). The results from opposite actuators were averaged to obtain single axial and circumferential stress–stretch curves. Instead of considering stretches and displacements at the level of the rakes, we determined the actual tissue stretches by planar particle tracking of the graphite-powder speckle pattern applied to the sample. Digital image correlation (DIC) was performed using VIC-2D software (Correlated Solutions, ISI-Sys, Irmo, SC) by analyzing the speckle pattern at a 20 Hz camera recording rate (Manta G-917, Allied Vision, Stadtroda, Germany) [12]. The center of the camera was aligned with the zero position of the actuators, imaging orthogonal to the middle of the sample. We consistently speckled and captured the intimal side of the artery. To ensure uniform sample strains, only the central 25% of the loaded area was considered [11,13].

The zero-strain state for each planar-biaxial stress–strain curve is defined as the point where both axial and circumferential stretches are unity ($\lambda_{ax} = \lambda_{circ} = 1$), and can be identified during postprocessing for each loading ratio by analyzing the last 50% loading curves. Specifically, we chose the planar-biaxial zero-strain state to correspond to the moment when the measured forces exceed a sample-specific predefined threshold. This tare load f_{pre} is determined at the start of the experiment by averaging the force values from the four load cells immediately after rake insertion. The mounted configuration is therefore assumed to be the best approximation of a flat, undeformed sample. As our protocol is displacement-driven, preconditioning will consistently lead to negative forces when the actuators move to their initial position and subsequently exceed the average mounting force or preload f_{pre}. Since the measured forces in the axial and circumferential directions are not independent, they share the same tare force to determine a unique zero-strain state for each loading ratio or test cycle. The choice of the tare load or zero-strain state is completely decoupled from the testing protocol, in order to prevent any preliminary assumptions during the planar-biaxial loading itself.

2.1.3 Opening Angle Measurements. Due to the release of residual stresses during planar-biaxial tissue specimen cutting, the reference state is different from the in vivo state. We performed opening angle tests on estimated 1 mm thick ring cuts to determine any circumferential prestretch in the arterial wall. The intact rings were submerged in 0.9% saline and scanned in a microlaser scanner (Acacia Technology & FIBEr, Leuven, Belgium). The rings were cut axially, submerged to reduce frictional forces, and ensuring complete residual stress release. A second scan allowed us to assess the sample-specific ring opening angle. All measurements were performed in the Gocator Emulator software (LMI Technologies, Vancouver, Canada).

The closed ring often had an elliptical shape instead of a perfect circle. The major and minor axes of a rectangular region box were manually adapted to match the inner side of the ring and averaged to determine a single value for the inner diameter R_i^{clos}, as shown in Fig. 3. The outer diameter of the closed ring (R_o^{clos}) is measured using the same method. For the open ring, inner and outer diameters (R_i^{open} and R_o^{open}) are measured using a circular sector-shaped bounding box. The sector region is delimited by lines extending from the center to the edges of the arc, with the opening angle β corresponding to the excluded arc angle. The inner diameter is the largest possible diameter within the open ring, and the outer diameter was taken at the same location.

A flattened square-shaped sample obtained from a curved tubular geometry theoretically introduces a flattening stretch and stress in the circumferential direction, unless the opening angle is 180 deg, which is assumed to be highly unlikely. For calcified arteries with a small opening angle, flattening could be substantial. However, in the considered carotid artery samples, the excised square samples flattened completely on their own when laid down freely. Moreover, flattening has been shown to minimally affect the inferred stress–strain pairs [14]. We therefore do not account for flattening effects when correlating the tubular geometry to planar-biaxial tissue testing in our workflow. Note that the sample is still unloaded in the axial direction in this configuration, and axial stretch and stress therefore remain unchanged.

closed ring measurements

inner diameter *outer diameter*

open ring measurements

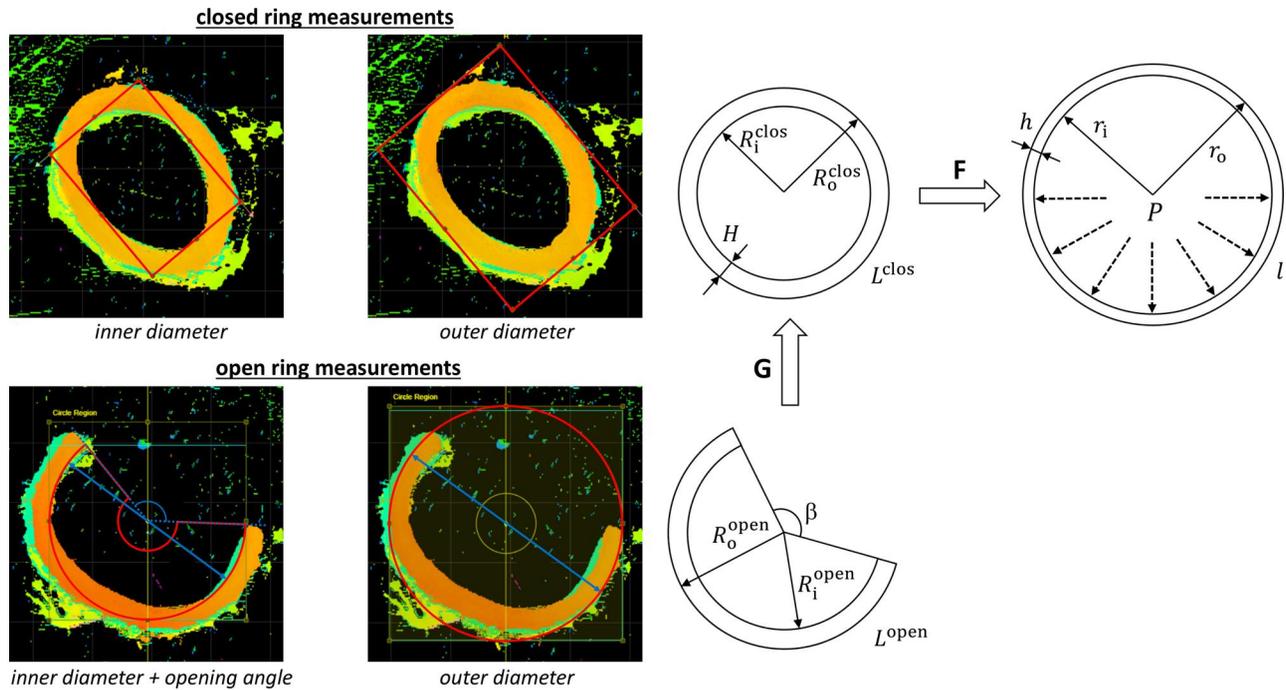*inner diameter + opening angle* *outer diameter*

Fig. 3 Ring-opening experiments to assess residual stresses and wall prestretches in tubular arterial tissue. The closed ring configuration was analyzed by fitting a rectangular bounding box to the tissue cross section, from which the inner and outer diameters (R_i^{clos} and R_o^{clos}) are computed, and the load-free wall thickness H can be derived. In the open ring configuration, β defines the opening angle. The inner diameter (R_i^{open}) is computed as the largest inscribed circle within the open ring, and the outer diameter (R_o^{open}) is measured at the same radial location. The prestretch tensor G links the reference configuration of length l^{clos} to a deformed configuration via the deformation gradient F. Axial stretch leads to a deformed length l and thickness h, with an inner pressure P inducing deformed diameters r_i and r_o.

2.1.4 Extension-Inflation Tests: Experimental Pressure–Diameter. The experimental extension-inflation tests were conducted using the ZwickRoell (Ulm, Germany) testing machine for *tubular* biomaterials. The device is controlled through a custom test environment created within the TESTXPERTII software. Two actuators of the machine are employed: (I) the linear displacement mechanism, oriented vertically, used for extending the sample and measuring the axial reaction force via a load cell, and (II) the pump, which is utilized to inflate the tubular sample, by pumping water into it, while simultaneously measuring the applied pressure.

To mount the sample, the top end is first fixed between a mounting pin and two mounting clamps, secured with four screws to ensure an airtight seal. The clamps have an axial length of 12 mm and an inner diameter of 4–6 mm, depending on the considered tube dimensions. The assembly lowered until the distance between the underside of the top clamps and the stud of the bottom mounting pin equals the initial axial hanging length of the tube sample. The bottom end of the sample is pulled over the bottom pin. The bottom of the tube is then clamped with similar mounting pieces and screws. The whole sample is submerged in a 0.9% saline solution by raising a 37 °C heated bath, and the axial load cell is zeroed. In the absence of axial forces, the measured distance between the clamps in this configuration is equal to the load-free sample length L^* (see Fig. 2).

Three consecutive load steps were performed, each applying a different axial stretch corresponding to 30%, 50%, and 75% of the initial mounted length. The mounted length is L^* measured with a caliper before testing, and is always smaller than the initial tube length L because of the 12 mm clamp dimension on each side. The ultimate axial stretch level of 75% represents physiological axial loading conditions for carotid arteries [15]. An internal pressure of 90 mmHg was applied during the first two axial stretch steps, while the physiological loading step was conducted at 180 mmHg. The latter reflects the upper limit of systolic blood pressure regimes [16]. Lower pressures were used in the initial steps to mitigate the risk of

premature tube sealing, loosening, or rupture. Axial loading was applied at a rate of 2.5%/s, and internal pressure was increased at a rate of 40.0 mmHg/s, with a pump speed of 3.5 nl/min volume. The relative pressure between the inside and outside of the sample is measured directly by the pressure sensor of the test device, with a precision 0.2% of the nominal value. In the extension-inflation test setup, we used an axial load cell of 20 N with a resolution of 67 μN.

The experimental outer diameter displacements are captured using a GRASSHOPPER3 camera (Teledyne FLIR, Wilsonville, OR). The imaging device is mounted horizontally and aligned with the center of the sample, with respect to both its length and its circumference. The camera, controlled by the VIC SNAP software, was configured at a recording rate of 20 Hz (Correlated Solutions, ISI-sys, Irmo, SC).

The outer diameter of the sample in the deformed configuration (d_o) is obtained by processing images captured by the camera in MATLAB (The MathWorks, Inc., Natick, MA). We differentiate the mounted, load-free outer diameter D_o, from the unpressurized but axially stretched outer diameter $d_o^{P=0}$, as highlighted for the measured tube in Table 1. We semi-automatically segmented each image to extract the sample and calculate the sample height and width in pixels. We convert pixels to millimeters using the pixel resolution, derived by dividing the known length or height of the mounted sample by the number of pixels in the sample length at the first image of the test protocol.

The converted width is recorded at various points along the sample length. To avoid boundary effects, resulting outer diameter values are reported for the middle of the sample, at equal distance from the proximal and distal clamp position. For the experimental pressure–diameter curves, we select the data from the 75% axial stretch loading condition. This step comprises five pressurization cycles, where the first four serve as preconditioning of the sample and minimize viscoelastic effects. Only the stretch or inflation part of the final cycle is used for analysis.of the artery

Table 1 Material parameters for sample B, including the unloaded experimental dimensions for the three geometries (square, ring, and tube), the fitted GOH material parameters, and the calculated prestretches obtained from the ring-opening experiments

Parameter	Definition	Value
Square $\rightarrow$ planar-biaxial		
W_1	Average sample width, axial direction	9.9 mm
W_2	Average sample width, circumferential direction	10.8 mm
T	Average sample thickness	0.30 mm
f_{pre}	Tare load	0.007 N
c_1	Neo-Hookean parameter	49.2 kPa
k_1	Fiber stiffness coefficient	5.3 kPa
k_2	Fiber stiffening coefficient	9.318
κ	Fiber dispersion	0.078
α	Fiber angle (with respect to the circumferential direction)	0.0 deg
Ring $\rightarrow$ ring-opening		
$R_{\mathrm{i}}^{\mathrm{open}}$	Inner radius, open ring	2.40 mm
$R_{\mathrm{o}}^{\mathrm{open}}$	Outer radius, open ring	3.15 mm
$R_{\mathrm{i}}^{\mathrm{clos}}$	Inner radius, closed ring	2.45 mm
$R_{\mathrm{o}}^{\mathrm{clos}}$	Outer radius, closed ring	1.83 mm
β	Opening angle	77°
$g_{\mathrm{circ,i}}$	Circumferential prestretch, inner wall	0.97
$g_{\mathrm{circ,o}}$	Circumferential prestretch, outer wall	0.99
g_{ax}	Axial prestretch	1.04
D_{o}	Load-free outer diameter	4.90 mm
H	Wall thickness	0.62 mm
Tube $\rightarrow$ extension-inflation		
L	Initial tube length	52 mm
L^*	Mounted length, measured	26.49 mm
$l^{P=0}$	Unpressurized length, axially loaded	46.14 mm
D_{o}	Mounted load-free outer diameter	5.49 mm
$d_{\mathrm{o}}^{P=0}$	Unpressurized outer diameter, axially loaded	4.99 mm
λ_{ax}	Applied axial prestretch	1.75

2.2 Modeling Workflow

2.2.1 Kinematics and Assumptions. In what follows, we will use uppercase notation to represent initial reference configurations, through Lagrangian variables X. Current or deformed configurations, and model parameters, will be represented by lowercase variables x. Tensors will be denoted in bold upright font, vectors in bold italic, and scalars in italic. Subscripts and superscripts representing indices will be italicized, while other subscripts and superscripts, such as abbreviations, will be written in upright font.

We define the deformation gradient as $\mathbf{F} = \partial \boldsymbol{x}/\partial \boldsymbol{X}$, where tissue incompressibility implies that the Jacobian $J = \det(\mathbf{F}) = 1$ [17,18]. We will highlight planar-biaxial configurations through subscript PB, while we will refer to extension-inflation setups as EI, resulting in pressure–diameter results (P–d). For consistency, we will write all modeled deformations as $\mathbf{F}^{\mathrm{mod}}$, and the corresponding modeled first Piola–Kirchhoff stresses as $\mathbf{P}^{\mathrm{mod}}$. Experimentally measured deformations and stresses will be denoted as $\mathbf{F}^{\mathrm{exp}}$ and $\mathbf{P}^{\mathrm{exp}}$, respectively.

In both the planar-biaxial test and the extension-inflation test, we ignore shear deformations. In the planar-biaxial test, we assume that the artery is consistently stretched in two perfectly orthogonal directions, aligned with the circumferential and axial directions of the artery. Using the stretch definition $\lambda = dx/dX$, we can write $\mathbf{F}_{\mathrm{PB}} = \mathrm{diag}\{\lambda_{\mathrm{circ}}, \lambda_{\mathrm{ax}}, \lambda_{\mathrm{rad}}\}$, in a Cartesian coordinate system, whereby the three principal directions align with the axial, circumferential, and radial directions of the artery, respectively. In the extension-inflation test, we assume an axisymmetric radial pressurization accompanied by an axial elongation, yielding a deformation gradient $\mathbf{F}_{\mathrm{EI}} = \mathrm{diag}\{\lambda_{\mathrm{rad}}, \lambda_{\mathrm{circ}}, \lambda_{\mathrm{ax}}\}$ in a cylindrical coordinate system. In both tests, the radial stretch is imposed by

incompressibility, $\lambda_{\mathrm{rad}} = \frac{1}{\lambda_{\mathrm{circ}} \lambda_{\mathrm{ax}}}$, whereas the circumferential and axial stretches will be imposed by the testing device.

We disambiguate stretch from strain by defining the nominal or engineering strain as $e = (dx - dX)/dX = \lambda - 1$.

2.2.2 Constitutive Model. Assuming hyperelastic material behavior, the Cauchy stress may be written as a function of the deformation as

$$\sigma = \frac{\partial \Psi(\mathbf{F})}{\partial \mathbf{F}} \mathbf{F}^T - p\mathbf{I}, \qquad (1)$$

where Ψ is the strain energy density function, and p is a Lagrange multiplier enforcing the incompressibility constraint, which will be determined by specific boundary condition assumptions of the planar-biaxial or extension-inflation setup. We can then calculate the corresponding first Piola–Kirchhoff stress (i.e., the transpose of the engineering stress) as $\mathbf{P} = J\sigma \mathbf{F}^{-T}$.

Based on literature, we choose to adopt the Gasser–Ogden–Holzapfel (GOH) strain energy density function for our arterial tissue, assuming Fung-type strain-stiffening fiber families embedded in an isotropic matrix [19–24]. From the right Cauchy–Green deformation tensor ($\mathbf{C} = \mathbf{F}^T \mathbf{F}$), we define the first and fourth strain invariants used in the GOH constitutive equation as $I_1 = \lambda_{\mathrm{circ}}^2 + \lambda_{\mathrm{ax}}^2 + (\lambda_{\mathrm{circ}} \lambda_{\mathrm{ax}})^{-2}$ and $I_4 = \lambda_{\mathrm{circ}}^2 \cos^2\alpha + \lambda_{\mathrm{ax}}^2 \sin^2\alpha$, respectively. λ_{ax} and λ_{circ} are again the principal stretches in the axial and circumferential direction. The angle α is defined as the collagen fiber orientation with respect to the circumferential direction in the circumferential–axial plane, assuming two symmetrically oriented

fiber families. Due to this symmetry, the fiber angle α is restricted to $0 \deg \leq \alpha \leq 90 \deg$. As such, the GOH model combines an isotropic neo-Hookean contribution based on the first invariant with an anisotropic fiber contribution of the fourth invariant, modeled by a quadratic-exponential function.

The resulting strain energy density function of the GOH constitutive model can be written as

$$\Psi_{\text{GOH}} = \frac{c_1}{2} [I_1 - 3] + \frac{k_1}{2k_2} \left(\exp\left(k_2 \left[I_4^* - 1 \right]^2 \right) - 1 \right), \quad (2)$$

with the shear modulus $c_1 > 0$, the stiffness-like parameter $k_1 > 0$ and the nondimensional coefficient $k_2 > 0$. The latter modulates the exponential strain-stiffening characteristics of the collagen fibers. The mixed isotropic–anisotropic fiber invariant term expands as $I_4^* = \kappa I_1 + (1 - 3\kappa)I_4$, where the microstructural fiber dispersion parameter κ modulates the degree of isotropy of the collagen fibers. When $\kappa = 0$, we have $I_4^* = I_4$, and the model reduces to non-dispersed collagen fibers along the direction defined by the angle α. When $\kappa = 1/3$, we have $I_4^* = I_1/3$, and the model reduces to a fully isotropic model.

2.2.3 Material Parameter Optimization. To identify the five optimal material parameters $\{c_1, k_1, k_2, \kappa, \alpha\}$ of the GOH model, we perform a parameter optimization using the `lsqnonlin` routine in MATLAB [25,26]. The optimization minimizes the two-norm of the residuals between experimental and model-predicted stress components

$$\min_{\theta} \sum_{r \in \mathcal{R}} \sum_{d \in \mathcal{D}} \left(P_{\text{PB}_{r,d}}^{\text{mod}} - P_{\text{PB}_{r,d}}^{\text{exp}} \right)^2, \quad \text{where } \theta = \{c_1, k_1, k_2, \kappa, \alpha\}. \quad (3)$$

The optimization combines the three loading ratios, $\mathcal{R} = \{1 : 1, 2 : 1, 1 : 2\}$, in the axial and circumferential direction, $\mathcal{D} = \{\text{ax}, \text{circ}\}$, considering the fifth loading cycle at 50% stretch. To balance the contributions of each experimental direction and loading ratio, we applied a scaling to normalize their magnitudes. Per sample, we weighted the error during fitting per ratio and per direction, in order to account for different data ranges equally. Moreover, we also compensated for the number of experimental data points per curve. Convergence to local minima was avoided by means of ten different initial guesses in a multistart strategy. The Lagrange multiplier p in $\mathbf{P}_{\text{PB}}^{\text{mod}}$ was calculated through the assumption of zero radial stresses, $P_{\text{rad}}^{\text{mod}} = 0$.

2.2.4 Simulating Pressure–Diameter Behavior. The analytical framework assumes a thick-walled, axisymmetric, cylindrical artery. The load-free configuration of an extension-inflation, at which $\mathbf{F}_{\text{EI}} = \mathbf{I}$, corresponds to the closed configuration at zero pressure, while the deformed state represents any pressurized configuration of the artery [27,28]. However, arterial tissue in a cylindrical tubular shape already finds itself in a prestretched state. Figure 3 shows the link between the deformation gradient $\mathbf{F}_{\text{EI}}$, and the prestretch tensor $\mathbf{G} = \text{diag}\left\{ g_{\text{circ}}, g_{\text{ax}}, \left(g_{\text{circ}} g_{\text{ax}} \right)^{-1} \right\}$, recalling the incompressibility constraint. $\mathbf{G}$ is used to disambiguate the undeformed load-free configuration from the reference stress-free configuration. From the opening angle β, we can compute

$$g_{\text{circ},j} = \frac{2\pi R_j^{\text{clos}}}{(2\pi - \beta) R_j^{\text{open}}} \quad (4)$$

at every integration point j through the thickness. A unique value of g_{ax} is iteratively found by matching the experimentally measured load-free thickness $H = R_o^{\text{clos}} - R_i^{\text{clos}}$ with the modeled radial coordinates through the thickness in the same reference configuration, , i.e., for an inner pressure $P = 0$ and an axial stretch $\lambda_{\text{ax}} = 1.0$.

The total deformation of the artery is then equal to $\mathbf{F}_{\text{EI}}^{\text{mod}} = \mathbf{F}_{\text{EI}} \mathbf{G}$, with the prestretch tensor $\mathbf{G}$ determined in the closed, load-free configuration, and the extension-inflation deformation gradient $\mathbf{F}_{\text{EI}}$ dependent on the applied inner blood pressure and imposed axial stretch. Since we assume a thick-walled cylinder, both tensors also vary along the arterial wall thickness.

Indeed, when applying a constant axial stretch $\lambda_{\text{ax}} = l/L^{\text{clos}}$, the remaining unknown in $\mathbf{F}_{\text{EI}} = \mathbf{F}_{\text{EI}}^{\text{mod}} \mathbf{G}^{-1}$ is $\lambda_{\text{circ}} = r/R$, which is dependent on the radial position. R_j and r_j can represent any corresponding undeformed and deformed radial coordinates in the arterial wall thickness. Consequently, we define $\lambda_{\text{circ},j}$, with j referring to a specific integration point through the wall. A blood pressure P is applied on the inside of the cylinder, with the outside pressure always taken as zero. By considering axisymmetric constraints and ignoring accelerations and body forces in the equation of balance of momentum $\nabla \sigma_{\text{EI}}^{\text{mod}} = 0$, the following equation for stress equilibrium in the radial direction can be derived [29]:

$$d\sigma_{\text{rad}} = (\sigma_{\text{circ}} - \sigma_{\text{rad}}) \frac{dr}{r}. \quad (5)$$

Integration over the wall, i.e., from the inner to the outer radius, and knowing that $\sigma_{\text{rad}}(r_o) = 0$ and $\sigma_{\text{rad}}(r_i) = -P$, yields

$$P_{\text{mod}} = \int_{r_i}^{r_o} (\sigma_{\text{circ}} - \sigma_{\text{rad}}) \frac{dr}{r}. \quad (6)$$

Consequently, the inner circumferential stretch $\lambda_{\text{circ},i}$ for any applied blood pressure P can be computed using following objective function:

$$\underset{\lambda_{\text{circ},i}}{\text{minimize}} \; \Delta P = P_{\text{mod}} - P = \int_{r_i}^{r_o} (\sigma_{\text{circ}} - \sigma_{\text{rad}}) \frac{dr}{r} - P. \quad (7)$$

An initial guess of $\lambda_{\text{circ},i}$ is required in the optimization scheme, and should be adjusted to match the expected deformations in order to enhance convergence over the complete pressure range. Volume conservation allows to derive $\lambda_{\text{circ},j} = r_j/R_j$ at any point in the wall. Indeed, due to incompressibility, it holds that

$$r_j = \sqrt{\lambda_{\text{circ},i}^2 R_i^2 + \frac{R_j^2 - R_i^2}{\lambda_{\text{ax}}}}. \quad (8)$$

Now, when calculating the modeled extension-inflation Cauchy stresses $\sigma_{\text{EI}}^{\text{mod}}$ through Eq. (1), the Lagrange multiplier p varies throughout the wall too. For the inner wall, it holds that $\sigma_{\text{rad}}(r_i) = -P$. Substitution yields an expression for p at the inner wall. Similarly, $\sigma_{\text{rad}}(r_o) = 0$. Therefore, to find the solution for the Lagrange multiplier within the wall, we consider that Eq. (5) should hold at every radial position. Thus

$$\sigma_{\text{rad}}(r_2) - \sigma_{\text{rad}}(r_1) = \int_{r_1}^{r_2} (\sigma_{\text{circ}} - \sigma_{\text{rad}}) \frac{dr}{r} \quad (9)$$

should hold for all radial positions r_1 and r_2 between the inner and the outer arterial wall, r_i and r_o. This allows us to obtain p at every radial position. Here, the integral was solved through 50 integration points and a trapezoidal method with equal spacing.

Solving Eqs. (6)–(8) allows us to derive the corresponding $\lambda_{\text{circ},o}^{\text{mod}}$ for any given pressure and applied axial stretch λ_{ax}, from which the resulting outer diameter d_o can be obtained. As such, we report the modeled pressure–diameter behavior for each specimen, over the range 0–200 mmHg.

The resulting axial Cauchy stress, averaged through the wall thickness, is equal to

$$\langle \sigma_{\text{ax}} \rangle = \frac{f_{\text{ax}}}{\pi \left(r_o^2 - r_i^2 \right)}, \quad (10)$$

where f_{ax} is the axial load on both ends of the tube in order to maintain the deformation [18]. Taking into account the contribution of the pressure on the end area of a tube with closed ends, we can then define the reduced axial force $f_{\mathrm{ax}}^{\mathrm{red}}$ as

$$f_{\mathrm{ax}}^{\mathrm{red}} = f_{\mathrm{ax}} - \pi r_{\mathrm{i}}^2 P. \qquad (11)$$

2.2.5 Extension-Inflation Optimization. From the modeled and experimental outer diameters, an additional optimization scheme can be performed through

$$\min_{\Theta} \left(d_o^{\mathrm{mod}}(\Theta) / d_o^{P=0}(\Theta) - d_o^{\mathrm{exp}} / d_o^{P=0} \right)^2 \qquad (12)$$

over the entire 0–200 mmHg pressure regime. We minimize the relative outer diameters by normalizing each value with respect to its unpressurized diameter. The pressure–diameter data from $\mathbf{F}_{\mathrm{EI}}^{\mathrm{exp}}$ or $\mathbf{F}_{\mathrm{EI}}^{\mathrm{mod}}$ is always considered at axial stretch λ_{ax}, i.e., at deformed length l. In the optimization procedure, an either-or approach is adopted, meaning that only one parameter, or subset of parameters, is optimized at a time, while the remaining variables are held fixed at their initial values listed in Table 1. Accordingly, different optimization schemes can be defined as

$$\Theta = \begin{cases} \theta & \text{if the GOH parameters are optimized,} \\ \lambda_{\mathrm{ax}} & \text{if the axial stretch is optimized,} \\ \beta & \text{if the opening angle optimized.} \end{cases}$$

Recall that θ is the set of GOH parameters, $\theta = \{c_1, k_1, k_2, \kappa, \alpha\}$.

3 Results and Discussion

In what follows, we will systematically present the results according to our workflow by first reporting the planar-biaxial stress–stretch experimental curves in the axial and circumferential direction. We overlay the experimental results with the simulated planar-biaxial curves computed by the Gasser–Ogden–Holzapfel (GOH) constitutive model fitting. Subsequently, the extracted material parameters are used to simulate the modeled pressure–diameter response of an idealized cylindrical geometry,

and to compare the results with experimental extension-inflation data. We then investigate the capacity of the GOH parameters to fit the extension-inflation data directly, and finally assess the sensitivity of the axial stretch λ_{ax} and opening angle β.

Due to the large variability between biological subjects and the sample-dependency inherent in our workflow, statistical analysis was deemed inappropriate. Instead, a single sample was selected as a use case and proof-of-concept for our data analysis. The Appendices contain the results for all the remaining samples.

3.1 Biaxial Fitting With Gasser–Ogden–Holzapfel Material Model. The resulting experimental engineering stress and DIC-derived stretch curves for the three loading ratios, based on the final loading cycle after preconditioning, are presented for representative sample B in Fig. 4. Table 1 reports the undeformed square dimension of the planar-biaxial sample, used to transform measured actuator forces into first Piola–Kirchhoff stresses. The biaxial square dimensions and GOH material parameters for samples A to E are reported in Appendix Table 2.

According to Sec. 2.2.2, the material parameters for the GOH constitutive model can be fitted to calculate the modeled stresses, $\mathbf{P}_{\mathrm{PB}}^{\mathrm{mod}}$, in the corresponding strain regimes. $R^2 = 0.908$ gives an indication of the goodness of fit between the experimental and modeled stress–stretch curves per sample, for the two directions and three loading ratios combined. The model's axial and circumferential predictions for the three loading ratios are overlaid with the corresponding experimental curves, demonstrating the model's ability to capture the anisotropic hyperelastic mechanical behavior of the arterial tissue. From Fig. 4, we note an observably stiffer experimental mechanical behavior in the circumferential direction with respect to the axial direction, consistent with the resulting GOH material parameters. Indeed, both modeled collagen fiber families were found to be oriented predominantly in the circumferential direction, exhibiting a small fiber dispersion. The latter is in agreement with microstructural fiber analysis in arteries, with a probability density function of collagen orientations toward the circumferential direction, despite a large spread and uncertainty [30].

Retrieving high-quality and biofidelic experimental planar-biaxial data is challenging. The observed tissue deformations are considerably lower than the nominal 50% stretch applied at the
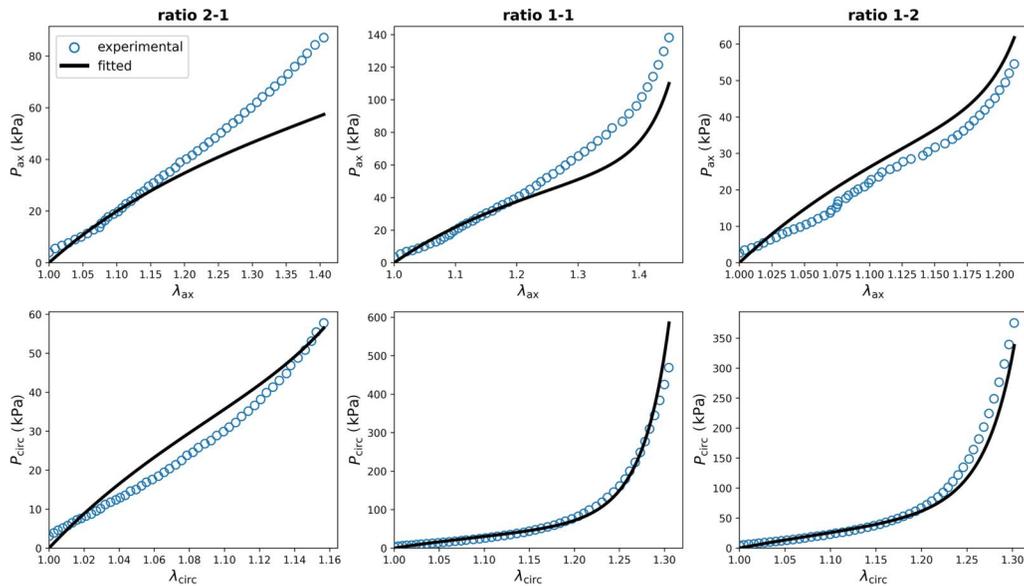

Fig. 4 Axial and circumferential first Piola–Kirchhoff stresses (P_{ax} and P_{circ}) plotted for sample B under three loading protocols with stretch ratios of 2:1, 1:1, and 1:2 in the axial and circumferential directions (λ_{ax} and λ_{circ}). Experimental stress–stretch data are shown alongside the modeled stress responses obtained using the fitted material parameters of the GOH constitutive model. The goodness of fit between modeled and experimental biaxial data of the three ratios and two directions is given by $R^2 = 0.908$.

rakes. This discrepancy arises from two factors: the actual strains at the center of the sample are smaller than those at the rakes [11], and our methodology to define the zero-strain state. Indeed, the initial starting point of the stress–stretch curve is set at the average force recorded by the four load cells immediately after mounting, prior to the onset of preconditioning. This approach provides the best available approximation of a flat, unstressed planar-biaxial tissue configuration. A fixed preload of 0 N should be avoided because of inevitable mounting forces. Defining zero-strain at higher forces would shift the origin of the stress–stretch curve even further along the loading axis, thereby omitting an additional portion of the low-strain response and overestimating tissue extensibility. Inelastic deformations could be present in part of the loading protocol, both during preconditioning and the main loading sequence. This is further evidenced by negative force values observed when the rakes return to their initial positions. Occasional discontinuities in the experimental stress–stretch curves are present, particularly in regions where the DIC strain measurements appeared challenging due to lighting, speckle tracking errors, or local sample deformations. The latter is also highlighted by a small but acceptable amount (<10%) of undefined values in the DIC-derived stretches. These limitations underscore the difficulty in obtaining clean, artifact-free biaxial data from soft biological tissues.

The fiber-dispersed GOH material model fits planar-biaxial arterial data well. Through the material parameter optimization of Eq. (3), the fiber-reinforced GOH model achieves an overall fitting performance of $R^2 > 0.8$ for all samples, indicating a consistent good fit between experimental data and the model stress–stretch predictions. Notably, the isotropic matrix stiffness parameter c_1 appears to scale with the exponential strain-stiffening coefficient k_2 of the collagen fibers, while the fiber stiffness parameter k_1 exhibits an inverse trend. This suggests a compensatory behavior between the isotropic and anisotropic components of the model. The fitted fiber direction of both collagen families is entirely oriented along the circumferential direction ($\alpha = 0 \deg$), but an axial stiffness contribution is introduced through a nonzero dispersion parameter ($\kappa > 0$). While this captures physiologically plausible mechanical behavior, it can also reveal over-parametrization of the GOH model in certain cases [24]. Actually, the structural parameters α and κ could be derived from microstructural analysis, such as second harmonic imaging through multiphoton microscopy. However, literature has shown that it remains challenging to accurately determine collagen fiber angles and dispersions in arterial tissue [31]. Alternatively to the conventional GOH model, constitutive artificial neural networks can be implemented to autonomously learn material behavior from the biaxial stress–stretch data [32–36]. This data-driven framework bypasses predefined model assumptions, and provides additional insights into stress–stretch behavior, offering a powerful alternative for capturing complex arterial mechanics. Instead of relying on the GOH strain energy density function, we explored automated model discovery in the Appendices (Fig. 18), and reported an updated constitutive description for carotid arteries.

3.2 Comparing Pressure–Diameter Responses. In this section, we analyze the pressure–diameter relation, Fig. 5(a), as well as the relative circumferential stretch, Fig. 5(b). The circumferential stretch in the extension-inflation plot is defined as the relative outer diameter, and computed as $d_o/d_o^{P=0}$. Both the current and initial diameter are computed in a deformed axial stretch state, i.e., with an applied λ_{ax}. Table 1 reports the experimental length and outer diameter of the tube, together with the ring measurements used to retrieve the model's load-free diameters and corresponding wall thickness at zero pressure. The tube dimensions and ring measurements for samples A to E are given in Appendix Table 3. We report the measured opening angles and corresponding circumferential prestretch at the inner and outer wall of the rings, together with their corresponding axial prestretch g_{ax}. Unless otherwise stated, the absolute and relative modeled curves are always calculated and plotted with an applied $\lambda_{ax} = 1.75$.
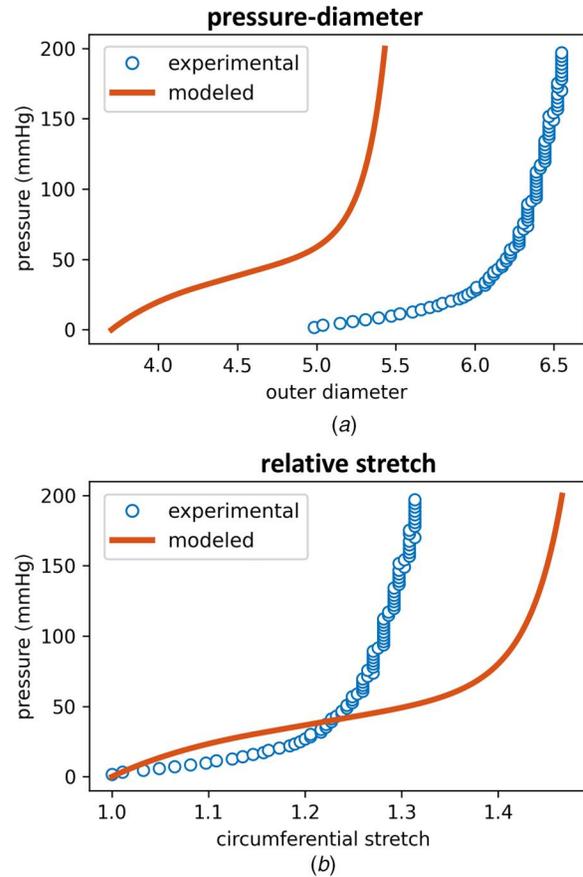

Fig. 5 Modeled and experimental pressure–diameter behavior for sample B, showing (*a*) the absolute outer diameter, and (*b*) the relative circumferential stretch. The modeled curves are generated using GOH material parameters fitted from the corresponding biaxial stress–stretch data. Experimental pressure–diameter data is extracted from the extension-inflation test.

The modeled curves underestimate the absolute pressure–diameter behavior. Figure 5(a) highlights how the model underestimates the absolute diameter values for almost all samples, except sample E. To get a sense of biofidelity of our results, the P–d curves could potentially be validated using in vivo imaging data, providing diameter measurements at diastolic and systolic pressures. However, such a validation protocol is challenging, as typically only inner diameters can be extracted from standard imaging data, and arterial blood pressures are often not recorded simultaneously with the imaging modality. Intravascular ultrasound has been used to measure both luminal diameters and pressurized arterial wall thicknesses, and may be further explored and implemented [37,38]. Pre-operative imaging of the sheep was not performed in this study, but the numerical values of the modeled absolute diameters are in agreement with literature data reported for ovine carotid arteries [39]. More specifically, inner diameters between 5 mm and 6 mm have been reported in the literature for systolic and diastolic blood pressures, which aligns well with our results. Normal diastolic and systolic arterial blood pressure values in sheep range from 60–80 mmHg and 90–120 mmHg, respectively [16]. This corresponds to the highly nonlinear exponential regime in our P–d curves, leading to only minor diameter changes and thus a limited pulsatile effect.

The modeled curves overestimate the relative pressure–circumferential stretch behavior. Figure 5(a) shows that the zero-pressure diameter does not coincide: the axially stretched but pressure-free outer diameter in the model is consistently lower than the experimentally measured outer diameter, even after an axial stretch of $\lambda_{ax} = 1.75$. The model's initial outer diameter and load-

free wall thickness are a potential cause of this mismatch, as the closed-ring configuration is a direct input of the simulations, without taking the tube dimensions into account. To overcome this inherent bias, we assess the pressure–diameter behavior in a relative manner through the circumferential stretch in Fig. 5(b). The latter was obtained by normalizing the diameter profile with its unpressurized but axially loaded value. Here we see that the model generally overestimates the relative diameter change compared to the experimental extension-inflation data. The best relative agreement between model and experiment is observed for samples C and D, see Appendix Figs. 12 and 13.

Probing relevant physiological stretches remains challenging. Ideally, we aim to reproduce the physiological stretch regime of arteries during biaxial testing, as this will enhance the biofidelity of the mechanical characterization and any downstream modeling or simulation steps. From in-house experiments at the Experimental Cardiac Surgery lab at KU Leuven on similar ovine carotids, we measured an in vivo axial length of approximately 3.5 cm reducing to an *ex vivo* length of around 2 cm, suggesting an axial stretch (λ_{ax}) of about 1.75. Furthermore, in vivo echo-ultrasound imaging of a carotid artery under pulsatile pressure showed a loaded inner diameter ranging between 4.5 and 5.5 mm, and a load-free inner diameter between 3.5 and 4 mm, corresponding to estimated circumferential stretches between 1.3 and 1.4. However, achieving such high deformation ranges is limited by experimental constraints, especially the failure of the rakes or clamping system at large displacements. Figure 6 shows how the arterial tissue was loaded in a very different axial-to-circumferential stretch domain when comparing planar-biaxial results with extension-inflation data. The experimental stretches show how $\mathbf{F}_{PB}^{exp}$ and $\mathbf{F}_{EI}^{exp}$ differ, and none of the biaxial stretch ratios come close to the extension-inflation deformations. The axial and circumferential components of the prestretch tensor in $\mathbf{F}_{EI}\mathbf{G}$ determine the reference configuration of the extension-inflation data ($\lambda_{ax} = \lambda_{circ} = 1$). Figure 6 nicely shows the absence of any relative axial stretch during pressurization. Indeed, experimentally, the clamps prevent axial movement and theoretically, the model predicts a constant axial deformation of $\lambda_{ax}g_{ax} \approx 1.82$.

Model predictions are influenced by both the planar-biaxial dataset and the constitutive description. Equation (3) considers the three axial-to-circumferential stretch ratios from the planar-biaxial dataset. To test if only a selected loading ratio would be more appropriate for accurately representing the in vivo loading conditions of a carotid artery, Figs. 14–16 in the Appendices assess the GOH material fitting and model predictions solely based on one of the 2:1, 1:1, or 1:2 planar-biaxial ratio. Based on the experimental measurements mentioned above, the axial-to-circumferential stretch ratio 2:1 approximates the best the biaxial stretch regime that the sample experiences during extension-inflation. However, this omits the strain-stiffening mechanical behavior of the collagen fibers in the circumferential direction from the planar-biaxial material fitting. When performing material parameter fitting based on planar-biaxial $\lambda_{ax} \rightarrow 1.4$ and $\lambda_{circ} \rightarrow 1.2$, the pressure–diameter model predictions therefore don't accommodate the exponential mechanical signature of an extension–inflation test (see Appendix Fig. 14). Planar-biaxial ratios 1:1 and 1:2 both reach $\lambda_{circ} \rightarrow 1.4$ and result in a nonlinear mechanical signature of the stress–stretch curve, but do not represent a physiological loading condition. Extrapolation of the fitted GOH model and parameters contributes to the poor pressure–diameter match when predicting extension-inflation data, as the simulation uses constitutive parameters fitted on mechanically nonphysiological planar-biaxial tensile tests. Rake failure at increased stresses prevented us from extending the stretch regime to $\lambda_{ax} \rightarrow 1.75$ and $\lambda_{circ} \rightarrow 1.375$, but future planar-biaxial testing protocols and loading ratios should be designed to experimentally reach those tissue-specific in vivo loading conditions [40].

In what follows, we will discuss possible solutions to the observed pressure–diameter offsets by refitting the GOH parameters to the extension-inflation data directly and analyzing the sensitivity of the axial stretch and circumferential prestretch.

3.3 Parameter Optimizations.
This section will explore how different modeling strategies and parameter choices can influence the accuracy of simulated pressure–diameter behavior for specimen B. To do so, we performed a least squares optimization of the modeled outer diameters over the whole pressure regime, see Eq. (11). Figure 7 compares several approaches and results. In particular, we will look into an alternative GOH parameter optimization, fitted to the extension-inflation data directly. We will then analyze the sensitivity of the modeled axial stretch and implemented ring opening angle, which influences the circumferential prestretch of the tissue.

3.3.1 Constitutive Parameter Fitting Based on Extension-Inflation.
Because the GOH parameters are fitted to planar-biaxial test data, which loads the considered square samples in a very different strain regime compared to the extension-inflation deformations, this leads to nonbiofidelic extrapolation of the results. Therefore, we here fit the GOH model directly onto the pressure–diameter data, through the optimization in Eq. (11), for the set of GOH parameters $\theta = \{c_1, k_1, k_2, \kappa, \alpha\}$, and with $\lambda_{ax} = 1.75$.

The GOH model can closely match experimental pressure–diameter relations as well as planar-biaxial data, but not simultaneously. Directly fitting the GOH model to the experimental extension-inflation data (Fig. 7(a)) greatly improves the agreement between the relative outer diameter of the model and the experiment. The changes in predicted pressure–diameter behavior originate from notably different fitted material parameters. The shear modulus c_1 decreases drastically, while the fiber stiffness parameter k_1 increases by nearly two orders of magnitude. Additionally, the exponential parameter k_2 increases sharply from 0.0932 to 11.38, indicating a much stronger strain-stiffening effect in the fiber direction. These parameter shifts underscore that planar-biaxial and extension-inflation tests probe fundamentally different aspects of the tissue's mechanical response. This is in line with previous research relating *ex vivo* triaxial shear testing to in vivo pressure–volume loop data [41,42]. Nevertheless, both planar-biaxial and extension-inflation approaches here provide valuable insights into the behavior and influence of the GOH parameters under distinct loading scenarios. We
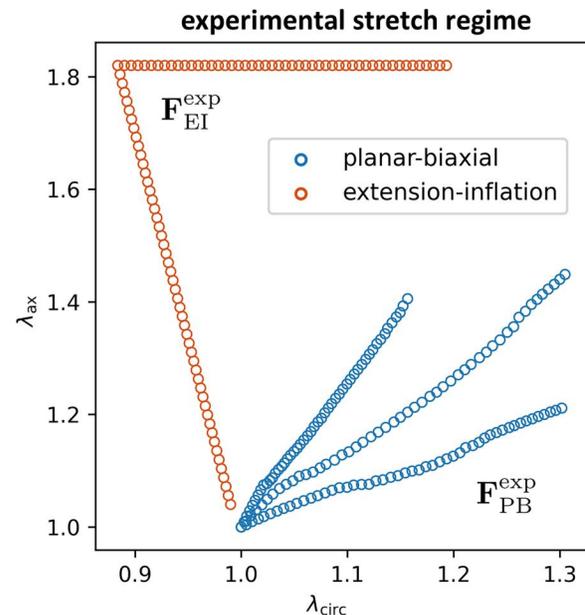

Fig. 6 Experimental biaxial stretch regimes. The three planar-biaxial axial-to-circumferential stretch ratios ($\mathbf{F}_{PB}^{exp}$) are plotted against the extension-inflation experimental deformations ($\mathbf{F}_{EI}^{exp}$). To maintain an equivalent reference configuration, the stretch domain of the extension-inflation test includes the prestretch tensor G, derived from the corresponding opening angle experiments.
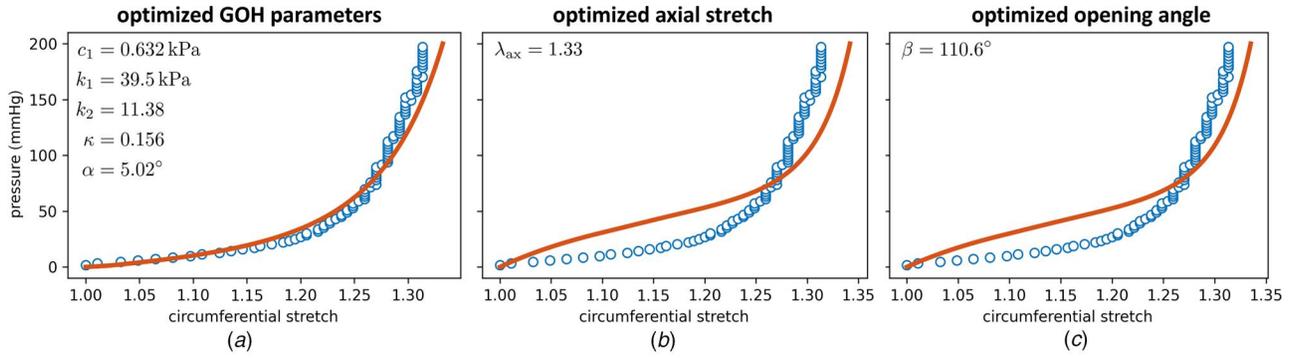
Fig. 7 Parameter optimizations to match experimental pressure–circumferential stretch behavior for specimen B: (a) GOH model fit directly on the extension-inflation data, (b) optimization of the axial stretch, and (c) optimization of the circumferential prestretch through the opening angle.

could also reevaluate the modeled planar-biaxial stress–stretch curves with the updated optimized GOH parameters from the extension-inflation data. Appendix Figure 17 shows an underestimation of the stress in the low-stretch regime, but an overshoot of modeled stress in the biaxial high-stretch regime. This overestimation is likely related to the collagen fiber stiffness and stiffening nonlinearity in the updated GOH material properties, dispersed around the circumferential direction, and required to meet the exponential pressure–diameter mechanical behavior.

The (an)isotropic balance of the GOH model has an important influence on the convex or concave shape of the pressure–diameter curve. The modeled GOH curve in Fig. 5(*a*) exhibits a pronounced concave slope at low pressures ($P < 50$ mmHg), transitioning into a highly nonlinear, convex diameter change as pressure increases,

characteristic of strain-stiffening behavior. In contrast, the experimental pressure–diameter curve displays a solely convex shape with an elongated toe region of approximately 20% stretch. When reducing the isotropic parameter c_1 of the GOH model while increasing the fiber-related parameters k_1 and k_2, the initial concave behavior of the P–d curve diminishes, resulting in a fully convex and exponentially increasing mechanical response in circumferential stretch (Fig. 7(*a*)). In Eq. (3), the five GOH parameters were scaled to account for relative importance, but a rigorous sensitivity analysis on the pressure–diameter results through Sobel indices could further reveal mutual influence.

3.3.2 Axial Stretch Analysis. The influence of the axial stretch on the model predictions is given in Fig. 8. By varying λ_{ax} over a physiologically relevant domain from 1.0 to 2.0, we can observe
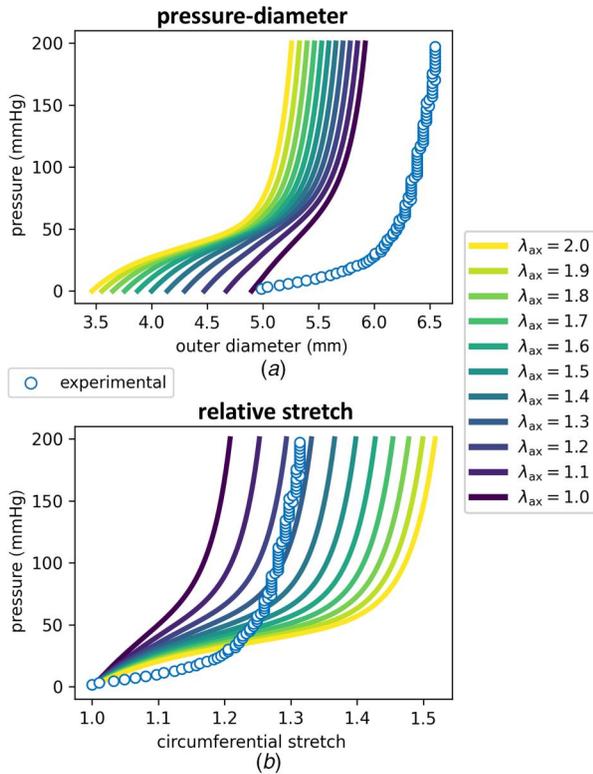

Fig. 8 Sensitivity of model predictions to the axial stretch for specimen B. Axial stretch values range from 1.0 to 2.0 in increments of 0.1. (a) Modeled pressure–diameter curves for each axial stretch value (b) Corresponding relative circumferential stretch behavior. The experimentally applied axial stretch during extension-inflation testing was $\lambda_{ax} = 1.75$, as imposed by the device actuator.
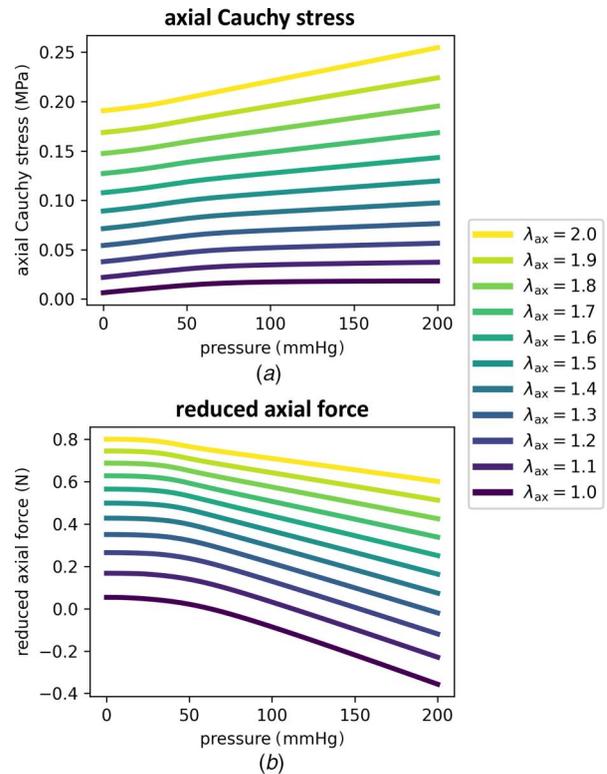

Fig. 9 Axial loading conditions at different axial stretches for specimen B. (a) Resulting axial Cauchy stress $\langle \sigma_{ax} \rangle$, averaged through the wall thickness. (b) Calculated reduced axial force f_{ax}^{red}. The experimentally applied axial stretch during extension-inflation testing was $\lambda_{ax} = 1.75$. The optimized axial stretch is $\lambda_{ax} = 1.33$.

clear changes in predicted pressure–diameter and circumferential stretch behavior. In Fig. 9, we introduce the resulting effects on mean axial Cauchy stress and reduced axial force across blood pressures.

Increasing the axial stretch reduces absolute diameters but increases the circumferential deformation. Increasing the modeled axial stretch leads to a decrease in the absolute modeled outer diameter (Fig. 8(*a*)), while simultaneously increasing the relative circumferential stretch regime (Fig. 8(*b*)). However, increasing axial stretch values to supra-physiological ranges will ultimately result in a severe increase in tissue stiffness and a reversal of the trend. Indeed, $\lambda_{ax} > 2.5$ will cause the relative diameter curve to shift leftwards again with increasing pressures. Ultimately, and in the specific case of sample B here, $\lambda_{ax} \approx 3.75$ will match the experimental curve again. However, such an axial stretch range is far above the experimentally observed and reasonable in vivo values of λ_{ax}. A similar relative outer diameter optimization in Eq. (11) can be performed to find the optimal axial stretch. Figure 7(*b*) therefore retains the initial GOH parameters from Table 1 but optimizes λ_{ax}, resulting in a value of $\lambda_{ax} = 1.33$. The remarkable lower axial stretch improves model performance without refitting material constants, highlighting that uncertainties in axial boundary conditions of the tubes can have a strong influence on the model's accuracy.

Axial loading should be included in extension-inflation parameter optimizations. The optimization scheme could be enriched with axial data by normalizing Eq. (11) with the diameters before axial loading, $d_o^{P=0,\,\lambda_{ax}=1}$. In fact, one should also consider the measured axial forces during the extension-inflation experiment in order to perform a parameter optimization on actual biaxial loading conditions. Appendix Figure 11 reports the experimentally measured axial forces during the extension-inflation of sample B. Calculated for physiological pressures and at $\lambda_{ax} = 1.75$, we added the modeled values of f_{ax}. For the range of varying axial stretches,
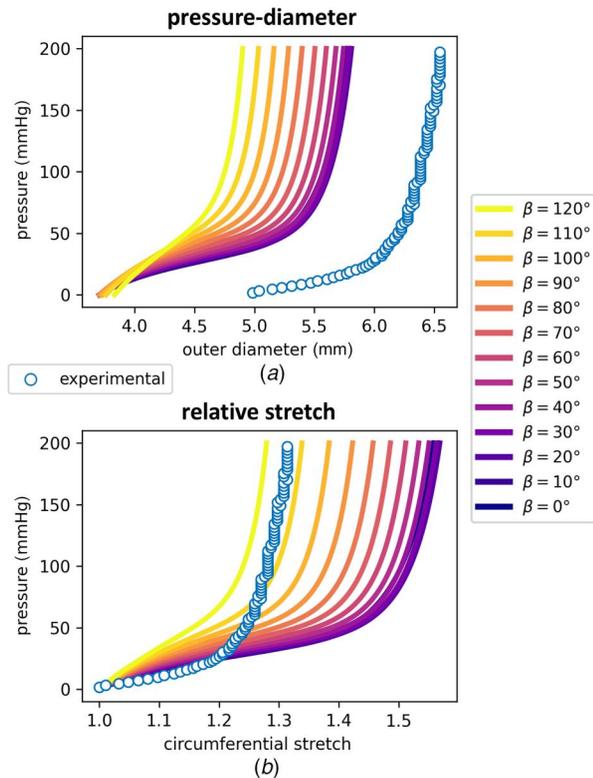

pressure-diameter

relative stretch

Fig. 10 Sensitivity of model predictions to the opening angle for specimen B. The opening angle ranges from 0 deg to 120 deg in increments of 10 deg. (*a*) Modeled pressure–diameter curves for each opening angle value. (*b*) Corresponding relative circumferential stretch behavior. The experimentally measured opening angle is β=77 deg.

Figs. 9(*a*) and 9(*b*) show the modeled Cauchy stress $\langle\sigma_{ax}\rangle$ and calculated the reduced axial load f_{ax}^{red}, based on Eqs. (9) and (10), respectively. For increasing values of λ_{ax}, the axial wall stress profile shifts from decreasing to increasing pressure response and is inversely proportional to the reduced axial force. The axial stretch analysis demonstrates how sensitive wall stress estimation is to longitudinal loading and highlights the importance of the experimental tube assumptions in the pressure–diameter predictions. In the literature, the most physiological axial stretch is often defined as the value at which the axial load remains nearly constant, despite an increase in intimal blood pressure [43]. The latter hypothesis is that smooth muscle cells in the arterial wall seek axial steadiness but circumferential pulsatility.

3.3.3 Opening Angle Analysis. The effect of the opening angle is illustrated in Fig. 10. By systematically varying the opening angle β from 0 deg to 120 deg, we assess how residual circumferential prestretch impacts the model's mechanical predictions for absolute and relative outer diameters. The opening angle effect demonstrates the importance of the excised rings in the model workflow and its predictive influence.

Increasing the opening angle stiffens both the absolute and relative pressure–diameter curves. An increasing opening angle causes a stiffening of the pressure–diameter response, both in absolute values and in relative deformation (Figs. 10(*a*) and 10(*b*)). A larger opening angle implies greater residual stress at zero pressure, effectively preloading the vessel wall in the circumferential direction. As a result, the tissue deforms less under pressurization, leading to a stiffer mechanical response. For sample B, the experimentally measured opening angle was $\beta = 77$ deg, which aligns well with the model's predicted behavior in this intermediate stiffness range. Importantly, the sensitivity of model predictions to variations in β suggests that incorporating accurate residual stress measurements is essential when simulating vascular mechanics. Unlike the tubular axial stretch, which is externally imposed during testing, the opening angle reflects intrinsic tissue architecture retrieved from ring opening experiments, and should thus carefully be considered during model calibration. Through Eq. (11), we perform an optimization of the optimal opening angle on the experimental extension–inflation data. Figure 7(*c*) retains the initial GOH parameters of Table 1 with $\lambda_{ax} = 1.75$, and finds the opening angle and thus circumferential prestretch that minimizes the relative outer diameter difference. This results in a value of $\beta = 110.6$ deg, leading to circumferential prestretches of $g_{circ,i} = 1.09$ and $g_{circ,i} = 1.12$, at the inner and outer wall, respectively. Our initial model was thus based on a underestimation of the opening angle. The resulting circumferential prestretches are calculated through Eq. (3), and therefore, highly dependent on the open and closed ring diameters, as well as the wall thickness H. An opening angle of $\beta = 110.6$ deg leads to an updated axial prestretch $g_{ax} = 0.78$, ensuring a match in the experimental and modeled load-free thickness for $P = 0$ and $\lambda_{ax} = 1.0$.

3.4 Geometrical Uncertainty. In addition to the GOH material parameters, the axial stretch and circumferential prestretch, several other geometrical quantities remain uncertain across the different load-free and loaded configurations. These uncertainties are briefly discussed in the following section.

The measured load-free thickness and reference diameters are inconsistent in different configurations. Table 1 shows a discrepancy between the mounted outer diameter of the tubes, D_o, and the measured outer diameter from the excised rings, $2R_o^{clos}$. The mismatch could originate from the fact that the ring dimensions were measured at anatomical positions more distal or more proximal to the experimental tubes (Fig. 2), leading to sample-specific biological intravariability. A clinical validation could include a comparison between the in vivo arterial wall thicknesses and the modeled values of h, expressed in the deformed configuration, see Fig. 10. The unpressurized wall thickness used in the predictive model, derived from the closed rings and defined as

$H = R_\mathrm{o}^\mathrm{clos} - R_\mathrm{i}^\mathrm{clos}$, is notably larger than the experimental thickness T measured from the squared biaxial sample (Table 1), which was used to calculate the planar-biaxial stress tensor $\mathbf{P}_\mathrm{PB}^\mathrm{exp}$. However, a thinner wall will intuitively result in even larger pressurized diameters, due to reduced resistance to circumferential expansion. The concave shape at low pressures remained because of the unaltered GOH parameters in this step.

Experimental pressure–diameter data should be enhanced with in vivo measurements. To obtain an exact and sample-specific axial stretch estimation, one should measure the arterial length l before explantation, and the excised length L^clos of the same tissue *ex vivo*, resulting in an estimation of λ_ax. According to Fig. 3, the same axial measurement could be performed on the open ring L^open, in order to obtain the experimental $g_\mathrm{ax}^\mathrm{exp}$. The experimental axial prestretch could then be compared to the modeled value in Table 1 to verify the workflow. However, in the current model workflow, the optimized g_ax guarantees computational consistency by ensuring a match between the experimental load-free closed ring configuration and the modeled geometry at $P = 0$ and $\lambda_\mathrm{ax} = 1.0$. However, biological variability might surpass experimental accuracy when measuring the difference between L^clos and L^open. An additional in vivo measurement could assess the diameter $d_\mathrm{o}^\mathrm{exp}$ at zero pressure, considering the unpressurized artery before sacrifice. The model can predict the same $d_\mathrm{o}^{P=0} = 2r_\mathrm{o}^{P=0}$ by solely applying the axial stretch λ_ax of the deformation gradient. The same diameter at zero pressure after axial loading is also used to normalize the results and compute the relative circumferential stretch curves. For $d_\mathrm{o}^{P=0}$ in Fig. 8(*a*), we also see that the experimental outer diameter from $\mathbf{F}_\mathrm{EI}^\mathrm{exp}$ is close to the modeled $\mathbf{F}_\mathrm{EI}^\mathrm{mod}$ at $\lambda_\mathrm{ax} = 1.0$.

Experimental extension-inflation requires advanced imaging and can suffer from clamping boundary condition effects. The experimental extension-inflation test setup and resulting experimental pressure–diameter curve could be improved in order to enhance the accuracy and reliability of the measurements. For instance, a dual-camera system could be installed to capture uniform and out-of-plane three-dimensional deformations using 3D-DIC, and to track the actual outer diameter of the pressurized test sample, rather than relying on a two-dimensional plane projection. In addition, the experimentally applied extension and inflation conditions are susceptible to error. The inflation pressure may be affected by leakage or offsets in the pressure regulation system, and the actual axial stretch experienced by the sample may differ from the nominal value of $\lambda_\mathrm{ax} = 1.75$ applied at the actuator level. The latter could be experimentally measured by marker tracking of the longitudinal axis extension. Pure pixel tracking of the sample height now shows $l^{P=0}/L^* = 1.74$, see Table 1. During internal pressurization, the measured diameter may vary along the length, typically exhibiting a barrel-shaped profile. This length-dependent diameter evolution originates from the limited sample availability, where the available carotid samples should be free of holes or defects along the required testing length to ensure reliable data. In the current study, only the diameter at the middle of the sample is extracted from the extension-inflation experiments, and the model assumes a straight, perfect cylindrical geometry. Incorporating the length-dependent diameter evolution into the analysis could provide a more accurate description of the deformation. In the optimization described by Eq. (11), the inclusion of a longitudinal dimension could then be considered to capture length-dependent effects on the diameter evolution. On the modeling side, the behavior of a hollow thick-walled cylinder under internal pressure, axial stretch, and radial constraints should also be examined. Such radial boundary conditions would introduce longitudinal stress variations and shear stresses in the radial-axial plane, which can induce bulging or deflation of the cylinder and must be accounted for in a comprehensive model of extension-inflation behavior.

Altogether, these results highlight the crucial interplay between accurate experimental measurements and endstage pressure–diameter results. While material calibration is key and essential, mismatches in the assumed wall thickness or vessel dimensions can propagate into model errors and obscure true mechanical behavior.

This emphasizes the need for careful geometric validation in conjunction with mechanical testing for reliable computational modeling of vascular tissues. The total experimental and model uncertainty, together with the variability of the geometries and model parameters, are therefore always important to consider. Literature presents different techniques to investigate this further [44–46].

4 Conclusions and Outlook

This study presents an integrated experimental and computational framework for characterizing ovine carotid artery biomechanics, bridging the gap between planar-biaxial testing and clinically relevant pressure–diameter behavior. We performed biofidelic extension-inflation experiments to compare model performance with benchtop pressure–diameter measurements. Our results highlight that translating laboratory measurements to realistic physiological conditions critically depends on accurately representing axial stretch and circumferential prestretch, as well as in vivo geometries. When these key parameters are well-characterized and their uncertainties properly accounted for, planar-biaxial stress–stretch data can become a reliable input for arterial pressure–diameter predictions.

We systematically combined planar-biaxial loading, ring opening experiments, and extension-inflation tests on the same arterial tissue. Squared, ring, and tubular samples of the same specimen allowed us to capture complementary loading conditions and holistically assess tissue behavior. To ensure physiological relevance, we designed and reported tailored experimental protocols with (I) controlled axial and circumferential loading in planar-biaxial tests, and (II) axial loading under luminal pressure in extension-inflation setups. To minimize measurement uncertainty, we employed digital image correlation for accurate deformation tracking and incorporated precise geometric data from microlaser scanning and ring-opening tests. These efforts improved the reliability of stress calculations and deformation measurements, thereby strengthening model input quality.

The modeling framework used the GOH constitutive model to capture the anisotropic hyperelastic material behavior of carotid arteries. Biomechanical predictions were performed through analytical thick-walled cylinder simulations with subject-specific tissue properties, boundary conditions, and prestretches. Robust validation was achieved by benchmarking simulated pressure–diameter behavior against experimental extension-inflation data from the same specimens. Systematic comparison of absolute and relative pressure–stretch responses revealed key discrepancies and highlighted the influence of parameter choices on model performance.

Our results confirmed that the in vivo stretch in carotid arteries is higher in the axial direction, while the tissue exhibits lower circumferential prestretches. The GOH model fitted the planar-biaxial data well and proved to be a suitable constitutive description for pressure–diameter simulations. Comparisons between experimental and simulated pressure–diameter curves showed a systematic underestimation of the absolute pressure behavior and overestimation of the relative circumferential stretch, where we found that the anisotropic balance of the GOH model significantly shaped the pressure–diameter curve.

We showed that the planar-biaxial stretch regime probes fundamentally different deformations compared to an extension-inflation test. We therefore fitted the GOH parameters directly to the pressure–diameter data, demonstrating the versatility of the constitutive parameters, depending on their biomechanical loading condition. Sensitivity analyses of the tubular axial stretches and ring opening angles emphasized their importance in accurate model calibration. While an increased axial stretch reduced the predicted absolute diameters, it increased the relative outer diameters. An increasing opening angle led to an overall stiffening of the pressure–diameter behavior. Optimizing the axial stretch and circumferential prestretch further enhanced the biofidelity of our simulations. Finally, we showed how axial loading is critical when

performing parameter optimizations based on extension-inflation data.

Despite the robustness of our approach, some limitations remain. Experimental noise, biological heterogeneity, and model simplifications contribute to uncertainty. Standardizing measurement protocols, improving accuracy in thickness and diameter measurements, and automating postprocessing workflows will help reduce variability. Future work should focus on (I) expanding datasets to quantify aleatoric and epistemic uncertainties, (II) incorporating clinical imaging data for further validation, (III) exploring 3D optical measurements and inverse modeling to refine experimental and modeling assumptions, (IV) applying constitutive artificial neural networks to autonomously discover novel strain energy density functions for carotid arteries, and (V) implement length-dependent diameter evolutions in the model, in order to consider longitudinal stress variations due to boundary condition effects.

Acknowledgment

Funding Data

Data Availability Statement

All source data, processing code, and results are available in KU Leuven's research data repository through the following link.[3]

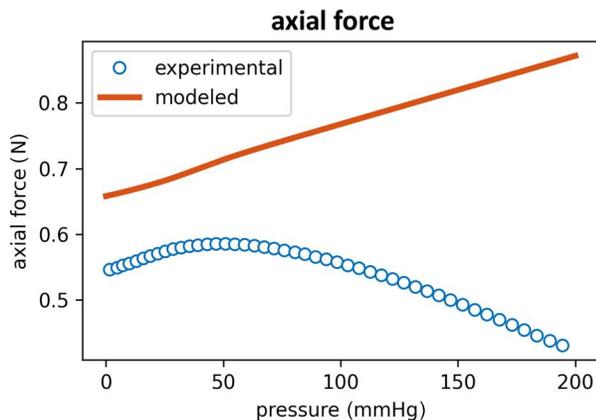## Appendix A: Supplementary Figures and Supplementary Tables

Fig. 11 Comparison of experimentally measured axial forces with the modeled-predicted values of f_{ax}. The results are plotted for the physiological extension-inflation pressure range of sample B, and at an axial stretch of $\lambda_{ax} = 1.75$.

[3]https://doi.org/10.48804/3SI2PR

Appendix B: Constitutive Artificial Neural Networks

Instead of relying on a predefined strain energy density function, we explore automated model discovery by training a constitutive artificial neural network (CANN). In this approach, we extend the set of strain invariants to include the isotropic second invariant $I_2 = \lambda_{circ}^{-2} + \lambda_{ax}^{-2} + (\lambda_{circ}\lambda_{ax})^2$ and the anisotropic fifth invariant $I_5 = \lambda_{circ}^4 \cos^2\alpha + \lambda_{ax}^4 \sin^2\alpha$. In the first layer of the neural network, we allow both the invariants and their squares, $(\cdot)$ and $(\cdot)^2$, as inputs. The second layer applies the identity function $(\cdot)$ and the exponential function $\exp(\cdot)$ to these transformed inputs. The layers are interconnected by carefully designed activation functions that ensure thermodynamic consistency, material objectivity, symmetry, physical restrictions, and polyconvexity [32]. Together, the neural network architecture gives rise to the following generalized strain energy density function:

$$
\begin{aligned}
\Psi_{\text{CANN}} = {}& w_1 w_1^*[I_1 - 3] + w_2\left(\exp\left(w_2^*[I_1 - 3]\right) - 1\right) \\
& + w_3 w_3^*[I_1 - 3]^2 + w_4\left(\exp\left(w_4^*[I_1 - 3]^2\right) - 1\right) \\
& + w_5 w_5^*[I_2 - 3] + w_6\left(\exp\left(w_6^*[I_2 - 3]\right) - 1\right) \\
& + w_7 w_7^*[I_2 - 3]^2 + w_8\left(\exp\left(w_8^*[I_2 - 3]^2\right) - 1\right) \\
& + w_9 w_9^*[I_4 - 1] + w_{10}\left(\exp\left(w_{10}^*[I_4 - 1]\right) - 1\right) \\
& + w_{11} w_{11}^*[I_4 - 1]^2 + w_{12}\left(\exp\left(w_{12}^*[I_4 - 1]^2\right) - 1\right) \\
& + w_{13} w_{13}^*[I_5 - 1] + w_{14}\left(\exp\left(w_{14}^*[I_5 - 1]\right) - 1\right) \\
& + w_{15} w_{15}^*[I_5 - 1]^2 + w_{16}\left(\exp\left(w_{16}^*[I_5 - 1]^2\right) - 1\right), \quad \text{(B1)}
\end{aligned}
$$

The network has a total of two times 16 trainable weights, resulting in more than 65,000 possible combinations. The network can learn any strain energy function constructed from first- and second-order, as well as identity and exponential additive combinations of the invariants I_1, I_2, I_4, and/or I_5. We also fit the fiber angle α, influencing the contribution of both the anisotropic terms I_4 and I_5. More details on the network's architecture can be found in prior works [33,35,47].

Here, we use cross-sample feature selection to setup the loss function of $\Psi_{\text{CANN}}(I_1, I_2, I_4, I_5)$. We train the neural network on all planar-biaxial samples together, with the fifth loading cycle of the three stretch ratios. We train for 8000 epochs, with a batch size of 32. Early stopping is allowed within 2000 epochs of no accuracy change [48,49]. The adaptive Adam algorithm is used for first-order optimization. To prevent local minima effects, we initialize the weights of the neural network layers with random values drawn from a uniform distribution. Specifically, the Glorot normal initializer is used for the identity functions, and an unseeded random uniform initialization is used for the exponential functions, with a minimum and maximum weight value of 0.0001 and 0.1, respectively [33].

We enforce the weights to always remain non-negative, $w \geq 0$. L1 or Lasso regularization can induce additional sparsity by reducing some weights exactly to zero, which effectively reduces model complexity and improves interpretability [50]. Here, we set the parameter α_{reg} to 0.01 to activate regularization.

With our set of weights $w = \{w_1^*, ..., w_{16}^*, w_1, ..., w_{16}\}$ we perform a gradient descent learning on a weighted least-squares error loss function L, penalizing the error between the discovered planar-biaxial model $\mathbf{P}_{\text{PB}}^{\text{mod}}$ and the experimental planar-biaxial data $\mathbf{P}_{\text{PB}}^{\text{exp}}$ as

$$
\begin{aligned}
L\left(w; \mathbf{F}_{\text{PB}}^{\text{exp}}\right) = {}& \sum_{n_{\text{smp}}} \frac{1}{n_{\text{data}}} \sum_{n=1}^{n_{\text{data}}} \left\| \frac{\mathbf{P}_n^{\text{mod}} - \mathbf{P}_n^{\text{exp}}}{P_{\text{smp,rat,dir}}^{\max}} \right\|^2 \\
& + \alpha_{\text{reg}} \sum_{k=1}^{16} \left(|w_k^*| + |w_k|\right) \to \min_{w}, \quad \text{(B2)}
\end{aligned}
$$

where n_{data} is the total number of data points of a specific sample, considering the three axial-verses-circumferential experimental loading ratios $\{1:1, 2:1, 1:2\}$, and the two loading directions:

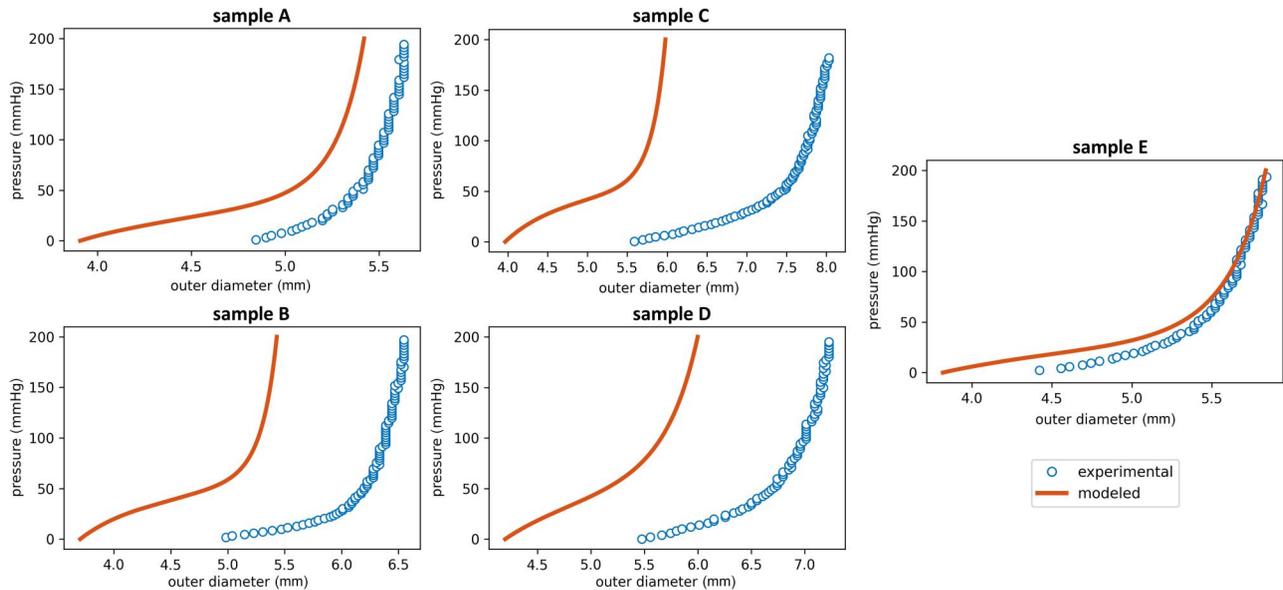**Fig. 12   Modeled and experimental pressure–diameter (P–d) relationships for the five carotid artery specimens (A–E). The modeled curves are generated using GOH material parameters fitted from the corresponding biaxial stress–stretch data. Experimental pressure–diameter data is extracted from extension-inflation tests performed on each specimen.**
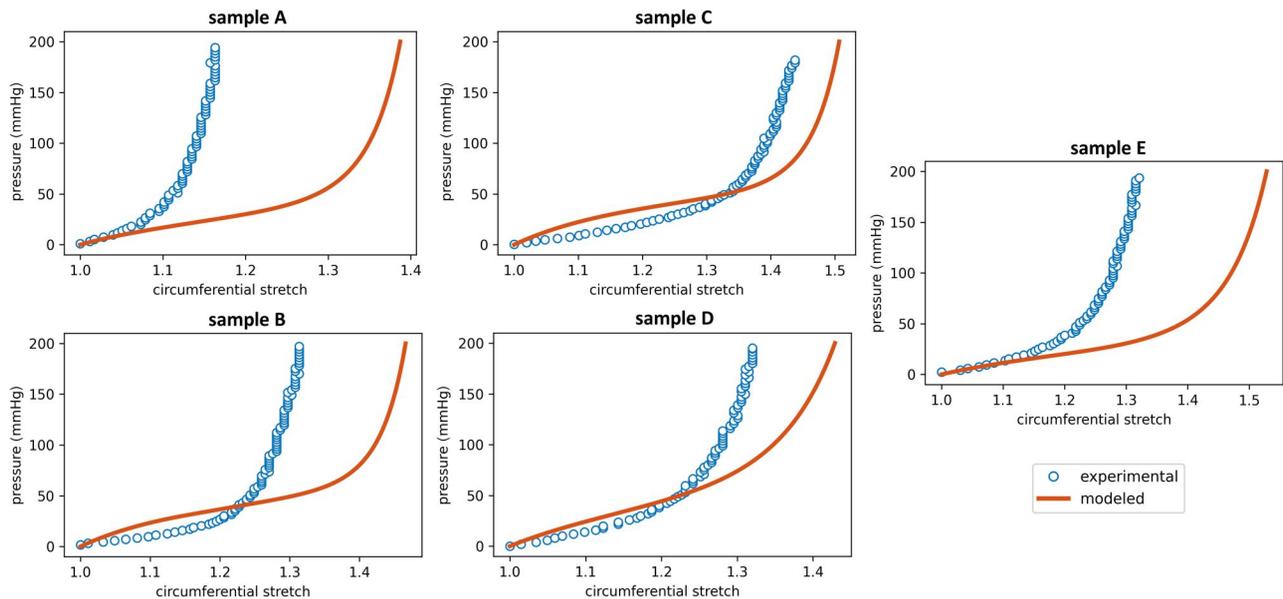

Fig. 13   Modeled and experimental pressure–circumferential stretch (P–λ_{circ}) relationships for the five carotid artery specimens (A–E). The modeled curves are generated using GOH material parameters fitted from the corresponding biaxial stress–stretch data. Experimental pressure–diameter data is extracted from extension-inflation tests performed on each specimen.

Table 2   Biaxial square dimensions and GOH material parameters $\theta = \{c_1, k_1, k_2, \kappa, \alpha\}$, fitted to the fifth loading cycle of biaxial tensile tests for samples A to E

	Squares (mm)			GOH parameters					
Sample	W_1	W_2	T	c_1 (kPa)	k_1 (kPa)	k_2	κ	α (rad)	R^2
A	10.5	10.6	0.43	28.4	7.0	6.259	0.112	0.000	0.874
B	9.9	10.8	0.30	49.2	5.3	9.318	0.078	0.000	0.908
C	10.9	9.7	0.23	67.2	3.0	12.268	0.134	0.000	0.796
D	10.3	10.7	0.31	31.2	18.9	6.469	0.186	0.000	0.853
E	10.7	10.9	0.57	20.8	7.8	6.595	0.136	0.000	0.883

The values W_1 and W_2 are the perpendicular widths of the axial and circumferential direction, respectively. T is the averaged wall thickness of the biaxial square sample measured through microlaser scanning. The goodness of fit of the modeled and experimental stress–stretch curves are highlighted by R^2.

Sample	Tubes (mm)			Rings (mm)				(deg)			
	L	D_o	$d_o^{P=0}$	R_i^{open}	R_o^{open}	R_o^{clos}	R_i^{clos}	β	$g_{circ,i}$	$g_{circ,o}$	g_{ax}
A	36	5.36	4.84	1.95	3.10	2.58	1.85	44	1.08	0.95	0.98
B	52	5.49	4.99	2.40	3.15	2.45	1.83	77	0.97	0.99	1.04
C	54	6.18	5.59	2.60	3.15	2.63	2.08	42	0.90	0.94	1.17
D	30	6.04	5.47	2.85	3.70	2.80	2.00	94	0.95	1.02	1.02
E	49	4.82	4.42	3.30	3.90	2.53	1.85	131	0.88	1.02	1.11

L represents the harvested axial length of the tubes. D_o highlights the mounted and unpressurized outer diameters, while $d_o^{P=0}$ describes the measured unpressurized outer diameters after applying the axial stretch λ_{ax}. R_i^{open} and R_o^{open} are the inner and outer radii of the ring in the open configuration, while R_i^{clos} and R_o^{clos} are the corresponding radii in the closed configuration. β is the opening angle in degrees, $g_{circ,i}$ and $g_{circ,o}$ are the resulting inner and outer circumferential prestretches, respectively, and g_{ax} is the optimized axial prestretch.

axial and circumferential, $\{ax, circ\}$. We extend the loss function with n_{smp} to account for the sample set from the different planar-biaxial tests. To account for all experiments equally, we weight the error with the maximum stress per ratio and per direction, and for each sample, with $P_{smp,rat,dir}^{max}$. This loss function allows us to discover a unique model or set of invariant features and find a universal constitutive behavior. In the absence of radial stresses during the planar-biaxial test, we define an explicit expression for the Lagrange multiplier p as a boundary condition for the incompressibility requirement.

Figure 18(a) demonstrates the CANN's ability to identify physically interpretable and directionally dependent components of arterial tissue mechanics. The learned strain energy function includes the linear isotropic contribution from the first invariant in the form of $[I_1 - 3]$, with weights $w_1 = 90.034$ kPa and $w_1^* = 0.090$, as well as the quadratic isotropic contribution of the first invariant $[I_1 - 3]^2$, with weights $w_3^* = 11.119$ kPa and $w_3 = 0.111$. An anisotropic exponential quadratic term $\exp([I_5 - 1]^2)$ is aligned with the circumferential direction (collagen fiber angle $\alpha = 0°$) and scales with weights $w_{15} = 2.373$ kPa and $w_{15}^* = 0.193$. The
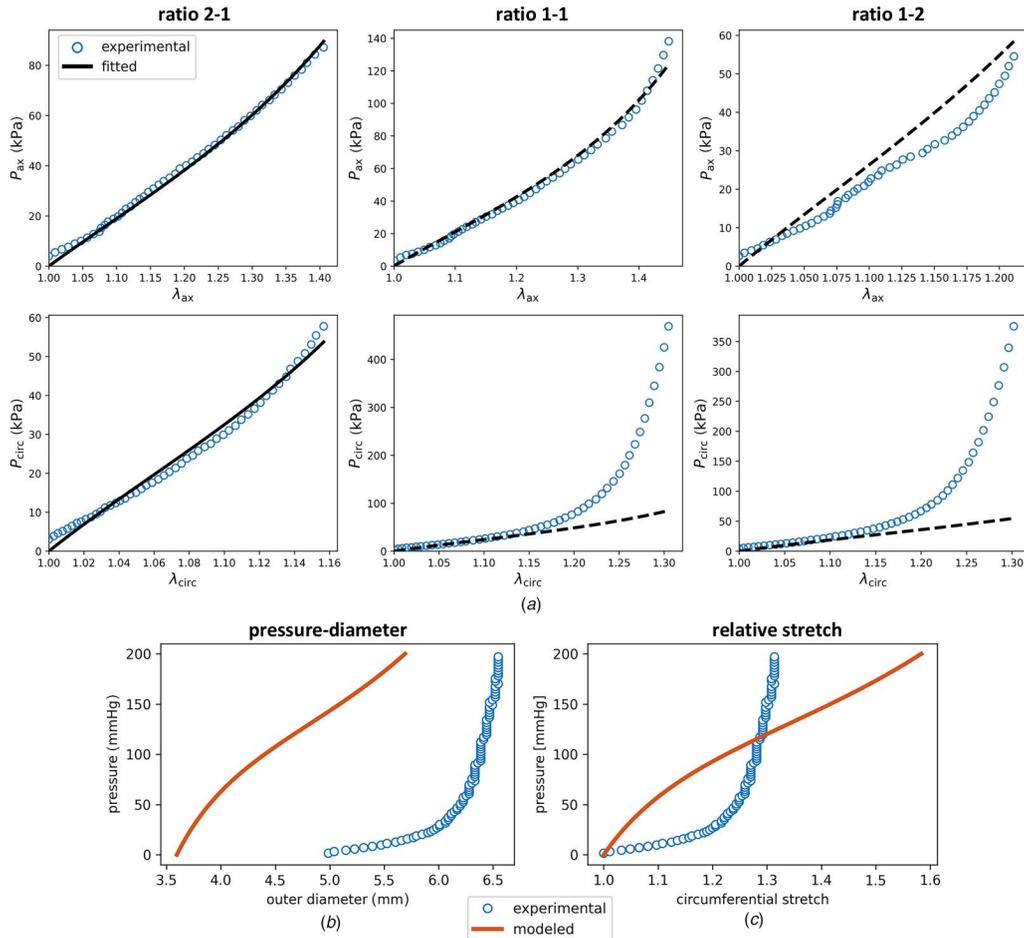

Fig. 14 Model predictions when the material parameters of the GOH model are fitted solely using the planar-biaxial data from the 2:1 axial-to-circumferential stretch ratio. The resulting material parameters for sample B are $c_1 = 35.2$ kPa, $k_1 = 8.2$ kPa, $k_2 = 5.5086$, $\kappa = 0.000$ and $\alpha = 0.2761$ rad. (a) Axial and circumferential stresses plotted under three loading protocols. Experimental stress–stretch data are shown alongside the fitted and predicted stress responses. (b) Resulting modeled and experimental absolute pressure–diameter behavior, and (c) corresponding pressure–circumferential stretch curves, showing relative deformation.

goodness of fit across samples can be assessed through the mean experimental curve, or by aggregating the planar-biaxial data of all $n = 5$ samples for the three ratios and two directions, resulting in an $R^2 = 0.631$, calculated w.r.t. the CANN-modeled stress–stretch curves ($\mathbf{P}_{PB}^{mod}$). Intuitively, R^2 is lower for cross-sample assessment, but previous work has shown that the neural network generally outperforms the GOH model [35]. The corresponding CANN weights indicate the relative importance of each term and reflect meaningful mechanical behavior, learned directly from the data. For carotid arteries, Eq. (B1) thus reduces to the following strain energy density function:

$$\Psi_{carotid} = w_1 w_1^*[I_1 - 3] + w_3 w_3^*[I_1 - 3]^2$$
$$+ w_{15}\left(\exp\left(w_{15}^*[I_5 - 1]^2 - 1\right)\right). \qquad (B3)$$

Figures 18(b) and 18(c) apply the discovered model to specimen B within the modeling framework. Using the learned invariant terms and weights, the model more accurately reproduces the absolute pressure–diameter response and closely matches the experimental outer diameters at diastolic and systolic carotid blood pressures. While the relative pressure–circumferential stretch behavior captures the general trend, it tends to overshoot more noticeably in the high-pressure regime. This can be attributed to the dominant contribution of the anisotropic exponential I_5 term, which is oriented solely in the circumferential direction and has a major influence in the physiological high-pressure regime of carotid arteries. In contrast, the isotropic I_1 term induces a concave mechanical behavior primarily in the low-pressure regime, capturing initial vessel response. Through automated model discovery, these result highlights the CANN's ability to uncover interpretable and predictive constitutive forms without predefined assumptions. It offers an attractive, data-driven pathway to model development in pressure–diameter simulations based on planar-biaxial datasets. We show that the constitutive neural network robustly discovers similar I_1 and I_5 invariant forms of arterial constitutive models for carotid arteries as observed in other pressurized cardiovascular tissues, such as human aortic arches or ovine main pulmonary arteries [35,47].
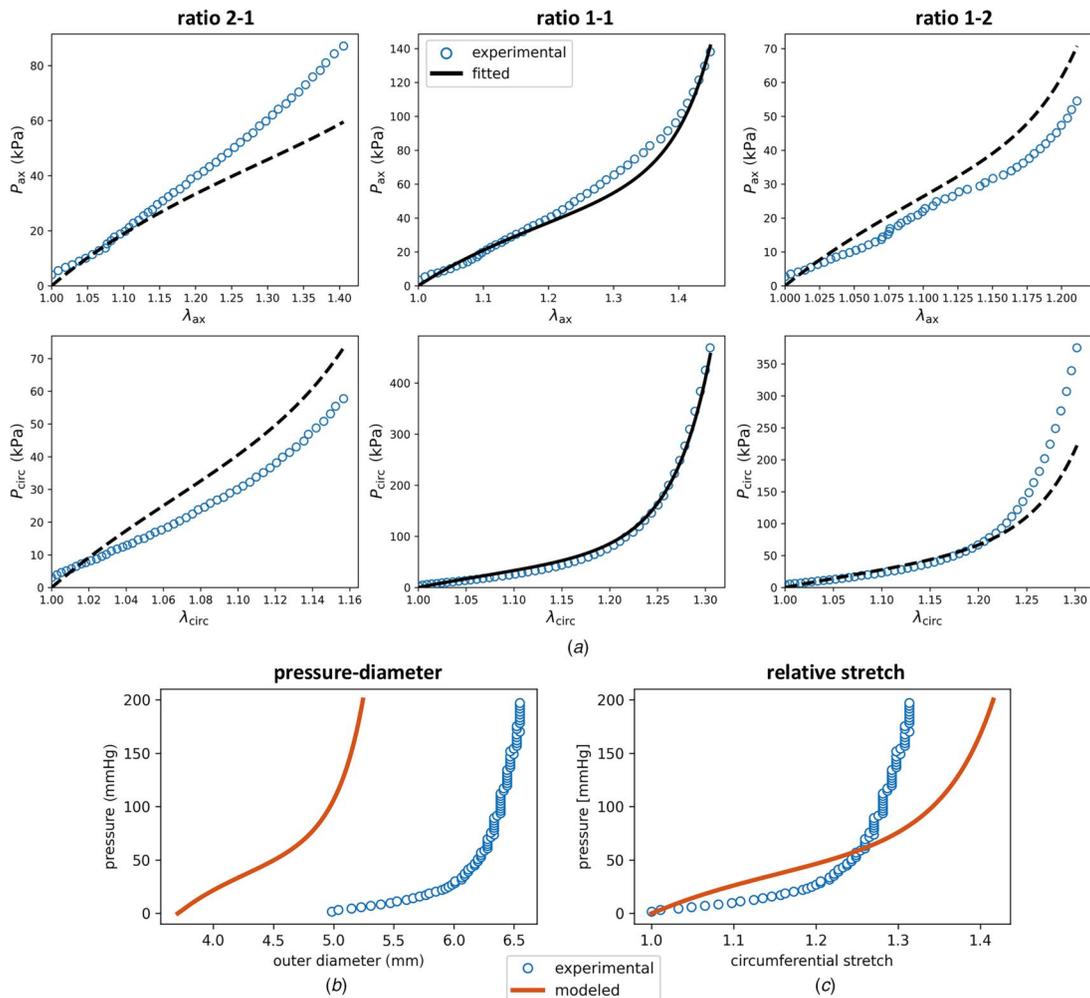

Fig. 15 Model predictions when the material parameters of the GOH model are fitted solely using the planar-biaxial data from the 1:1 axial-to-circumferential stretch ratio. The resulting material parameters for sample B are $c_1 = 45.2\,kPa$, $k_1 = 8.9\,kPa$, $k_2 = 4.4479$, $\kappa = 0.000$, and $\alpha = 0.4088\,rad$. (a) Axial and circumferential stresses plotted for sample B under three loading protocols. Experimental stress–stretch data are shown alongside the fitted and predicted stress responses, (b) resulting modeled and experimental absolute pressure–diameter behavior, and (c) corresponding pressure–circumferential stretch curves, showing relative deformation.
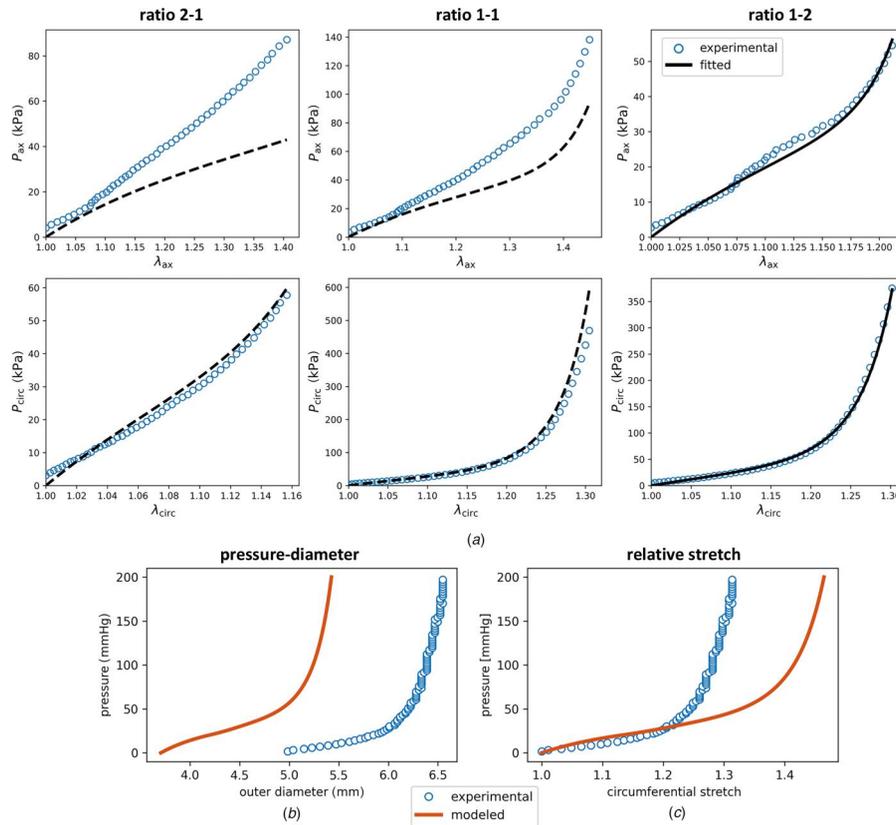
Fig. 16 Model predictions when the material parameters of the GOH model are fitted solely using the planar-biaxial data from the 1:2 axial-to-circumferential stretch ratio. The resulting material parameters for sample B are $c_1 = 37.4\,\text{kPa}$, $k_1 = 43.8\,\text{kPa}$, $k_2 = 0.8815$, $\kappa = 0.2358$ and $\alpha = 1.0515\,\text{rad}$. (*a*) Axial and circumferential stresses plotted under three loading protocols. Experimental stress–stretch data are shown alongside the fitted and predicted stress responses. (*b*) Resulting modeled and experimental absolute pressure–diameter behavior. (*c*) Corresponding pressure–circumferential stretch curves, showing relative deformation.
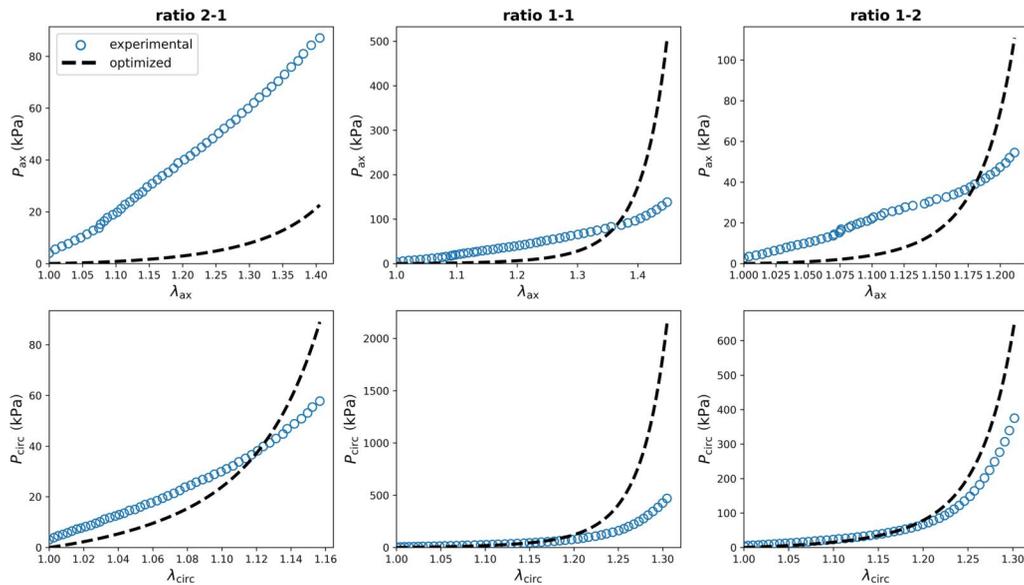

Fig. 17 Axial and circumferential first Piola–Kirchhoff stresses (P_{ax} and P_{circ}) plotted for sample B under three loading protocols with stretch ratios of 2:1, 1:1, and 1:2 in the axial and circumferential directions (λ_{ax} and λ_{circ}). Experimental stress–stretch data are shown alongside the virtual stress responses computed using the optimized material parameters of the GOH constitutive model ($c_1 = 0.632\,\text{kPa}$, $k_1 = 39.5\,\text{kPa}$, $k_2 = 11.38$, $\kappa = 0.156$, and $\alpha = 0.087\,\text{rad}$). These model parameters were obtained by fitting the GOH model directly to the pressure–diameter data from the experimental extension-inflation test (see Sec. 3.3.1 and Fig. 7(*a*)).
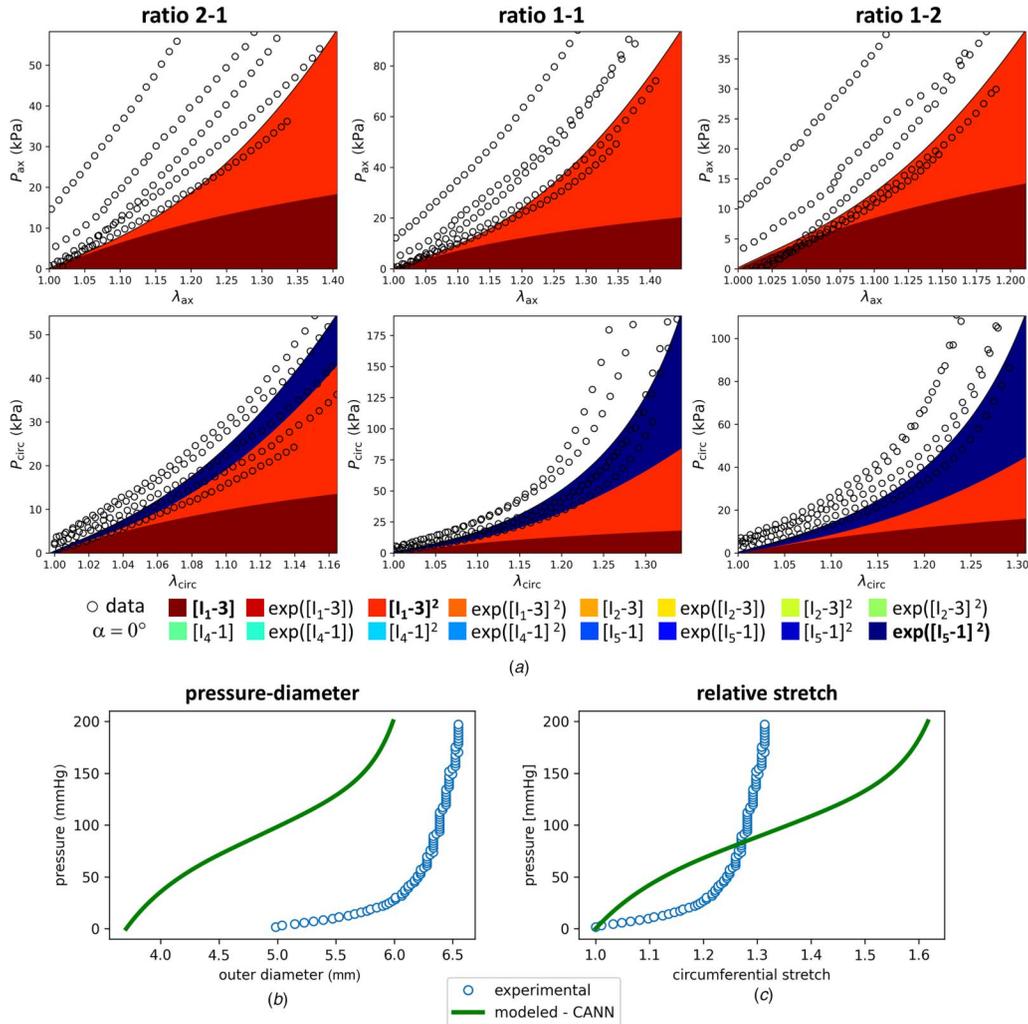
Fig. 18 Discovered material model for the constitutive artificial neural network (CANN) trained on the planar-biaxial stress–stretch data from the five carotid artery specimens combined and used to predict the pressure–diameter behavior. (*a*) The discovered strain energy function includes isotropic contributions from the first invariant in the form of $[I_1-3]$ and $[I_1-3]^2$, and a circumferential anisotropic fiber contribution represented by $\exp([I_5-1]^2)$. (*b*) Comparison of modeled and experimental absolute pressure–diameter behavior, where the discovered terms and learned weights are used to simulate the arterial wall response. (*c*) Corresponding pressure–circumferential stretch curves, showing relative deformation.

References

[1] Ramachandra, A. B., and Humphrey, J. D., 2019, "Biomechanical Characterization of Murine Pulmonary Arteries," J. Biomech., **84**, pp. 18–26.

[2] Smoljkić, M., Sloten, J. V., Segers, P., and Famaey, N., 2015, "Non-Invasive, Energy-Based Assessment of Patient-Specific Material Properties of Arterial Tissue," Biomech. Model. Mechanobiol., **14**(5), pp. 1045–1056.

[3] Liu, M., Liang, L., Sulejmani, F., Lou, X., Iannucci, G., Chen, E., Leshnower, B., and Sun, W., 2019, "Identification of In Vivo Nonlinear Anisotropic Mechanical Properties of Ascending Thoracic Aortic Aneurysm From Patient-Specific CT Scans," Sci. Rep., **9**(1), pp. 1–13.

[4] Boekhoven, R. W., Peters, M. F., Rutten, M. C., van Sambeek, M. R., van de Vosse, F. N., and Lopata, R. G., 2016, "Inflation and Bi-Axial Tensile Testing of Healthy Porcine Carotid Arteries," Ultrasound Med. Biol., **42**(2), pp. 574–585.

[5] Doyle, B. J., Cloonan, A. J., Walsh, M. T., Vorp, D. A., and McGloughlin, T. M., 2010, "Identification of Rupture Locations in Patient-Specific Abdominal Aortic Aneurysms Using Experimental and Computational Techniques," J. Biomech., **43**(7), pp. 1408–1416.

[6] Korte, C. L. D., Fekkes, S., Nederveen, A. J., Manniesing, R., and Hansen, H. R. H., 2016, "Review: Mechanical Characterization of Carotid Arteries and Atherosclerotic Plaques," IEEE Trans. Ultrason. Ferroelectr. Freq. Control, **63**(10), pp. 1613–1623.

[7] Vander Linden, K., Fehervary, H., Maes, L., and Famaey, N., 2022, "An Improved Parameter Fitting Approach of a Planar Biaxial Test Including the Experimental Prestretch," J. Mech. Behav. Biomed. Mater., **134**, p. 105389.

[8] López, M., Martínez, J., Matías, J. M., Vilán, J. A., and Taboada, J., 2010, "Application of a Hybrid 3D-2D Laser Scanning System to the Characterization of Slate Slabs," Sensors, **10**(6), pp. 5949–5961.

[9] O'Leary, S. A., Doyle, B. J., and McGloughlin, T. M., 2014, "The Impact of Long Term Freezing on the Mechanical Properties of Porcine Aortic Tissue," J. Mech. Behav. Biomed. Mater., **37**, pp. 165–173.

[10] Fehervary, H., Vastmans, J., Sloten, J. V., and Famaey, N., 2018, "How Important is Sample Alignment in Planar Biaxial Testing of Anisotropic Soft Biological Tissues? A Finite Element Study," J. Mech. Behav. Biomed. Mater., **88**, pp. 201–216.

[11] Fehervary, H., Smoljkic, M., Sloten, J. V., and Famaey, N., 2016, "Planar Biaxial Testing of Soft Biological Tissue Using Rakes: A Critical Analysis of Protocol and Fitting Process," J. Mech. Behav. Biomed. Mater., **61**, pp. 135–151.

[12] Vander Linden, K., Fehervary, H., Vastmans, J., and Famaey, N., 2023, "The Influence of Out-of-Plane Motion on the Deformation Measurement of Planar Biaxial Tests on Biological Soft Tissue," Mech. Res. Commun., **129**, p. 104099.

[13] Sacks, M. S., 2000, "Biaxial Mechanical Evaluation of Planar Biological Materials," J. Elasticity, **61**(1/3), pp. 199–246.

[14] Jadidi, M., Desyatova, A., MacTaggart, J., and Kamenskiy, A., 2019, "Mechanical Stresses Associated With Flattening of Human Femoropopliteal Artery Specimens During Planar Biaxial Testing and Their Effects on the Calculated Physiologic Stress–Stretch State," Biomech. Model. Mechanobiol., **18**(6), pp. 1591–1605.

[15] Blondel, W., Didelon, J., Maurice, G., Carteaux, J.-P., Wang, X., and Stolz, J.-F., 2001, "Investigation of 3-D Mechanical Properties of Blood Vessels Using a New In Vitro Tests System: Results on Sheep Common Carotid Arteries," IEEE Trans. Biomed. Eng., **48**(4), pp. 442–451.

[16] Almeida, D., Barletta, M., Mathews, L., Graham, L., and Quandt, J., 2014, "Comparison Between Invasive Blood Pressure and a Non-Invasive Blood Pressure Monitor in Anesthetized Sheep," Res. Vet. Sci., **97**(3), pp. 582–586.

[17] Holzapfel, G. A., and Weizsäcker, H. W., 1998, "Biomechanical Behavior of the Arterial Wall and Its Numerical Characterization," Comput. Biol. Med., 28(4), pp. 377–392.

[18] Ogden, R. W., 2017, *Nonlinear Continuum Mechanics and Modeling the Elasticity of Soft Biological Tissues With a Focus on Artery Walls*, Vol. 20, Springer Nature, Germany.

[19] Fung, Y. C., Fronek, K., and Patitucci, P., 1979, "Pseudoelasticity of Arteries and the Choice of Its Mathematical Expression," Am. J. Physiol.-Heart Circ. Physiol., 237(5), pp. H620–H631.

[20] Holzapfel, G. A., Gasser, T. C., and Ogden, R. W., 2000, "A New Constitutive Framework for Arterial Wall Mechanics and a Comparative Study of Material Models," JELAS, 61(1), pp. 1–48.

[21] Gasser, T. C., Ogden, R. W., and Holzapfel, G. A., 2006, "Hyperelastic Modelling of Arterial Layers With Distributed Collagen Fibre Orientations," J. R. Soc. Interface, 3(6), pp. 15–35.

[22] Holzapfel, G. A., and Ogden, R. W., 2009, "On Planar Biaxial Tests for Anisotropic Nonlinearly Elastic Solids. A Continuum Mechanical Framework," Math. Mech. Solids, 14(5), pp. 474–489.

[23] Holzapfel, G. A., and Ogden, R. W., 2010, "Constitutive Modelling of Arteries," Proc. Royal Soc. A Math. Phys. Eng. Sci., 466(2118), pp. 1551–1597.

[24] Holzapfel, G. A., and Ogden, R. W., 2025, "Modeling the Biomechanical Properties of Soft Biological Tissues: Constitutive Theories," Eur. J. Mech., A/Solids, 112, p. 105634.

[25] Fehervary, H., Vander Sloten, J., and Famaey, N., 2019, "Development of an Improved Parameter Fitting Method for Planar Biaxial Testing Using Rakes," Int. J. Numer. Methods Biomed. Eng., 35(4), p. e3174.

[26] Maes, L., Fehervary, H., Vastmans, J., Mousavi, S. J., Avril, S., and Famaey, N., 2019, "Constrained Mixture Modeling Affects Material Parameter Identification From Planar Biaxial Tests," J. Mech. Behav. Biomed. Mater., 95(March), pp. 124–135.

[27] Peirlinck, M., De Beule, M., Segers, P., and Rebelo, N., 2018, "A Modular Inverse Elastostatics Approach to Resolve the Pressure-Induced Stress State for In Vivo Imaging Based Cardiovascular Modeling," J. Mech. Behav. Biomed. Mater., 85, pp. 124–133.

[28] Vervenne, T., Maes, L., Van Hoof, L., Rega, F., and Famaey, N., 2023, "Drivers of Vascular Growth and Remodeling: A Computational Framework to Promote Benign Adaptation in the Ross Procedure," J. Mech. Behav. Biomed. Mater., 148, p. 106170.

[29] Holzapfel, G., and Ogden, R. W., 2017, *Biomechanics: Trends in Modeling and Simulation: Studies in Mechanobiology, Tissue Engineering and Biomaterials* (Studies in Mechanobiology, Tissue Engineering and Biomaterials), Springer Nature, Germany.

[30] Rolf-Pissarczyk, M., and Terzano, M., 2023, "SIMCor. Deliverable 8.4 - Validated Constitutive Models of the Vessel Wall (TUG, M26)," Zendo, https://zenodo.org/records/10931406

[31] Fata, B., Carruthers, C. A., Gibson, G., Watkins, S. C., Gottlieb, D., Mayer, J. E., and Sacks, M. S., 2013, "Regional Structural and Biomechanical Alterations of the Ovine Main Pulmonary Artery During Postnatal Growth," ASME J. Biomech. Eng., 135(2), p. 0210221.

[32] Linka, K., and Kuhl, E., 2023, "A New Family of Constitutive Artificial Neural Networks Towards Automated Model Discovery," Comput. Methods Appl. Mech. Eng., 403, p. 115731.

[33] Linka, K., Buganza Tepole, A., Holzapfel, G. A., and Kuhl, E., 2023, "Automated Model Discovery for Skin: Discovering the Best Model, Data, and Experiment," Comput. Methods Appl. Mech. Eng., 410, p. 116007.

[34] Linka, K., Holzapfel, G. A., and Kuhl, E., 2025, "Discovering Uncertainty: Bayesian Constitutive Artificial Neural Networks," Comput. Methods Appl. Mech. Eng., 433, p. 117517.

[35] Vervenne, T., Peirlinck, M., Famaey, N., and Kuhl, E., 2025, "Constitutive Neural Networks for Main Pulmonary Arteries: Discovering the Undiscovered," Biomech. Model. Mechanobiol., 24(2), pp. 615–634.

[36] Martonová, D., Leyendecker, S., Holzapfel, G. A., and Kuhl, E., 2025, "Discovering Dispersion: How Robust is Automated Model Discovery for Human Myocardial Tissue?," Biomech. Model. Mechanobiol., pp. 1–15.

[37] Wittek, A., Karatolios, K., Bihari, P., Schmitz-Rixen, T., Moosdorf, R., Vogt, S., and Blase, C., 2013, "In Vivo Determination of Elastic Properties of the Human Aorta Based on 4D Ultrasound Data," J. Mech. Behav. Biomed. Mater., 27, pp. 167–183.

[38] Drews, J. D., Pepper, V. K., Best, C. A., Szafron, J. M., Cheatham, J. P., Yates, A. R., Hor, K. N., et al., 2020, "Spontaneous Reversal of Stenosis in Tissue-Engineered Vascular Grafts," Sci. Transl. Med., 12(537), p. 6919.

[39] James, N. L., Milijasevic, Z., Ujhazy, A., Edwards, G., Jermyn, K., Mynard, J. P., and Celermajer, D. S., 2019, "The Common Carotid Artery Provides Significant Pressure Wave Dampening in the Young Adult Sheep," IJC Heart Vasc., 23, p. 100343.

[40] Avazmohammadi, R., Li, D. S., Leahy, T., Shih, E., Soares, J. S., Gorman, J. H., Gorman, R. C., and Sacks, M. S., 2018, "An Integrated Inverse Model-Experimental Approach to Determine Soft Tissue Three-Dimensional Constitutive Parameters: Application to Post-Infarcted Myocardium," Biomech. Model. Mechanobiol., 17(1), pp. 31–53.

[41] Peirlinck, M., Sack, K. L., De Backer, P., Morais, P., Segers, P., Franz, T., and De Beule, M., 2019, "Kinematic Boundary Conditions Substantially Impact in Silico Ventricular Function," Int. J. Numer. Methods Biomed. Eng., 35(1), p. e3151.

[42] Peirlinck, M., Sahli Costabal, F., Sack, K. L., Choy, J. S., Kassab, G. S., Guccione, J. M., De Beule, M., Segers, P., and Kuhl, E., 2019, "Using Machine Learning to Characterize Heart Failure Across the Scales," Biomech. Model. Mechanobiol., 18(6), pp. 1987–2001.

[43] Hu, J. J., Fossum, T. W., Miller, M. W., Xu, H., Liu, J. C., and Humphrey, J. D., 2006, "Biomechanics of the Porcine Basilar Artery in Hypertension," Ann. Biomed. Eng., 35(1), pp. 19–29.

[44] Vander Linden, K., Vanderveken, E., Van Hoof, L., Maes, L., Fehervary, H., Dreesen, S., Hendrickx, A., Verbrugghe, P., Rega, F., Meuris, B., and Famaey, N., 2023, "Stiffness Matters: Improved Failure Risk Assessment of Ascending Thoracic Aortic Aneurysms," JTCVS Open, 16, pp. 66–83.

[45] Gheysen, L., Maes, L., Caenen, A., Segers, P., Peirlinck, M., and Famaey, N., 2024, "Uncertainty Quantification of the Wall Thickness and Stiffness in an Idealized Dissected Aorta," J. Mech. Behav. Biomed. Mater., 151, p. 106370.

[46] Berggren, C. C., Jiang, D., Jack Wang, Y. F., Bergquist, J. A., Rupp, L. C., Liu, Z., MacLeod, R. S., Narayan, A., and Timmins, L. H., 2024, "Influence of Material Parameter Variability on the Predicted Coronary Artery Biomechanical Environment Via Uncertainty Quantification," Biomech. Model. Mechanobiol., 23(3), pp. 927–940.

[47] Peirlinck, M., Linka, K., Hurtado, J. A., Holzapfel, G. A., and Kuhl, E., 2025, "Democratizing Biomedical Simulation Through Automated Model Discovery and a Universal Material Subroutine," Comput. Mech., 75(6), pp. 1703–1723.

[48] Peirlinck, M., Hurtado, J. A., Rausch, M. K., Tepole, A. B., and Kuhl, E., 2025, "A Universal Material Model Subroutine for Soft Matter Systems," Eng. Comput., 41(2), pp. 905–927.

[49] McCulloch, J. A., and Kuhl, E., 2024, "Automated Model Discovery for Textile Structures: The Unique Mechanical Signature of Warp Knitted Fabrics," Acta Biomater., 189, pp. 461–477.

[50] McCulloch, J. A., St. Pierre, S. R., Linka, K., and Kuhl, E., 2024, "On Sparse Regression, Lp-Regularization, and Automated Model Discovery," Int. J. Numer. Methods Eng., 125, p. e7481.